

Waves in Random and Complex Media
IMPACT FACTOR = 4.853
<https://www.tandfonline.com/journals/twrm20>

Accepted March 5th 2022

COMPUTATION OF REACTIVE THERMOSOLUTAL MICROPOLAR NANOFLUID SAKIADIS CONVECTION FLOW WITH GOLD/SILVER METALLIC NANOPARTICLES

MD. Shamshuddin *

Department of Mathematics, Vaagdevi College of Engineering (Autonomous), Warangal-506005, Telangana State, India.

Email: shammaths@gmail.com; shamshuddin_md@vaagdevi.edu.in

M. Ferdows

Department of Applied Mathematics, Research Group of Fluid Flow Modeling and Simulation. University of Dhaka, Dhaka-1000, Bangladesh.

Email: ferdowsmohammad@yahoo.com

O. Anwar Bég

Professor and Director - Multi-Physical Engineering Sciences Group, Mechanical Engineering Department, School of Science, Engineering and Environment (SEE), University of Salford, Manchester, UK.

Email: O.A.Beg@salford.ac.uk; gortoab@gmail.com

Tasveer A. Bég

Engineering Mechanics Research, Israfil House, Dickenson Rd., Manchester, M13, UK.

Email: tasveerabeg@gmail.com

H. J. Leonard⁵

Multi-Physical Engineering Sciences Group, Mechanical Engineering Department, School of Science, Engineering and Environment (SEE), University of Salford, Manchester, UK.

Email: h.leonard@salford.ac.uk

*Corresponding author

Abstract: In the present study, a mathematical model is developed by combining the Tiwari-Das nanofluid formulation with the Eringen micro-morphic model to simulate the thermo-solutal natural convection chemically reacting micropolar nanofluid flow from a permeable stretching surface with non-uniform heat source/sink effects. The transformed ordinary differential equation boundary value problem features linear momentum, angular momentum, energy and species conservation boundary layer equations with appropriate boundary conditions. This ninth order nonlinear system is solved with Runge-Kutta 45 Fehlberg method (Maple **dsolve routine**). Several nanoparticles i.e., gold, and silver with aqueous base fluid are studied. The influence of the effect of the emerging parameters on the velocity, angular velocity, temperature, nanoparticle concentration, skin friction, couple stress, Nusselt number and Sherwood number distributions are visualized and tabulated. It is observed that Increasing volume fraction decreases velocity whereas it elevates microrotation, temperature and nanoparticle concentration. Nanoparticle concentrations are elevated for stronger destructive chemical reaction effect whereas they are suppressed with constructive chemical reaction. With greater micropolar boundary condition parameter, the velocity is elevated, microrotation but reduces temperature and thermal boundary layer thickness. Increasing nanoparticle volume fraction enhances both skin friction and couple stress but marginally reduces the Nusselt number. Finally, Au-water micropolar nanofluids achieve the highest skin friction and couple stress magnitudes, then Ag-water and finally Cu-water. Validation of solutions with earlier non-reactive studies in the absence of nanoparticle mass transfer are included.

Keywords: *Non-uniform heat source/sink; chemical reaction; Sakiadis flow; micropolar nanofluids; gold and silver nanoparticles.*

1. INTRODUCTION

Non-Newtonian materials processing constitutes a rich arena for mathematical modelling [1]. Many industrial processes feature significant rheological characteristics of working fluids which are fundamental to their performance. Examples include paints, smart coating, electroconductive polymer enrobing, hydrogels etc. The accurate simulation of manufacturing processes involving such fluids requires more elegant formulations than the classical Navier-Stokes Newtonian viscous model. Non-Newtonian constitutive models for polymeric materials processing are available in many diverse formulations including viscoplastic, viscoelastic, memory fluids etc., [2-4]. Khan *et al.* [5] employed the PTT (Phan-Phien-Tanner) viscoelastic model for optical fiber coating simulation. Zevallos *et al.* [6] employed both the Oldroyd-B and the FENE-P (Finitely Extensible Nonlinear Elastic-Peterlin) models for roll coating analysis, noting that the elastic stresses modify flow near the film splitting meniscus by reducing and eventually eliminating the recirculation present at low capillary number. Chang *et al.* [7] employed the Walters-B elastic-viscous short memory model to study unsteady species diffusion in polymeric Sakiadis flow with wall transpiration effects. Garg *et al.* [8] used the Reiner-Rivlin differential second order viscoelastic model to study Falkner-Skan flows of polymers. These models however ignored the microstructure of the non-Newtonian fluid. Eringen [9] first proposed the *theory of micropolar fluids* to describe liquids such as colloidal solutions, liquid crystals, fluids with additives, low concentration suspensions, blood etc. Physically, micropolar fluids belong to a larger family of much more complex non-Newtonian fluids, namely *micromorphic fluids* or “*simple microfluids*” which contain fluid elements with deformable microstructure, admitting intrinsic motion characteristics and possessing a *non-symmetrical* stress tensor. Micropolar fluids can sustain rotation with individual motions which support stress and body moments and are influenced by spin-inertia. A particular advantage of the micropolar model is that the classical Navier-Stokes model for Newtonian fluids can be retrieved as a special case. Micropolar fluids provide a significantly more amenable model for computation than general micromorphic fluids and can represent fluids consisting of rigid, randomly oriented (or spherical) particles suspended in a viscous medium (e.g., proteins, erythrocytes, leukocytes, polymeric suspensions, paints, sediments, slurries, fuels, pharmacological agents etc.) where the deformation of fluid particles is ignored. In micropolar fluid dynamics, the classical continuum and thermodynamics laws are extended with additional equations, which account for the conservation of micro inertia moments and the balance of first stress moments which arise due to the consideration of micro-structure in a fluid. Hence new kinematic variables (*gyration tensor, microinertia moment tensor*), and concepts of body moments, stress moments and micro-stress are combined with classical continuum fluid dynamics theory. Micropolar theory has been experimentally verified [10] and has been utilized successfully in many areas of engineering fluid mechanics. Representative studies include Hung *et al.* [11] (on hydrodynamic stability of gravity driven micropolar fluids), Gupta *et al.* [12] (heat transfer in contracting polymeric sheets), Chen *et al.* [13] (swirling disk flows in which Eringen’s micropolar parameter i.e. ratio of vortex and Newtonian dynamic viscosities was shown to stabilize the thin film flow), Shamshuddin *et al.* [14] (thermo-solutal oscillating Sakiadis flow), Sheremet *et al.* [15] (unsteady free convection in corrugated surface enclosures), Madhavi *et al.* [16] (enrobing heat protection shield flows for rocket geometries), Chiu *et al.* [17] (unsteady heat transfer in concentric spherical bodies), Chaube *et al.* [18] (electrokinetic propulsion in microfluidics), Ali *et al.* [19] (anti-fouling coating slime dynamics), Srinivas and Bég [20] (nuclear hydromagnetic duct heat transfer control), Akbar *et al.* [21] (cilia-generated pumping of physiological liquids), Bég *et al.* [22] (Hall ocean magnetohydrodynamic power generation generators), Hiremath *et al.* [23] (nanofluid flow external to heated cylinder), Hiremath *et al.* [24] (heat transfer in third-grade fluid flow from

isothermal vertical plate) and Reddy et al. [25] (third-grade flow over a vertical cylinder) . All these studies have verified the significant modification in momentum, heat and also mass transfer characteristics computed with micropolar theory and the significant deviation from Newtonian and simple non-Newtonian models. Further studies include Chand *et al.* [26] (convection in a layer of micropolar nanofluid), Yadav and Wang [27] (thermal transport in a porous layer saturated with non-Newtonian nanofluid) and Yadav [28] (convective rolls in a porous medium saturated with ananofluid).

A significant development in 21st century engineering has been the emergence of *nanomaterials*. Engineers are increasingly designing systems at the nanoscale and important progress has been made in nanotube-embedded gels, nano-lubricants, electro-conductive nanopolymers etc. An important sub-group of liquid nanomaterials is *nanofluids*. Introduced in the 1990s by Choi *et al.* [29], these complex fluids were developed primarily to achieve substantial improvements in thermal enhancement. They are synthesized by doping conventional working fluids e.g., water, polymers, ethylene glycol etc., with either metallic or carbon-based nanoparticles with average particle sizes below 100 nm. The resulting colloidal suspension achieves superior thermal conductivity, heat capacity and viscosity properties compared with macroscopic fluids. Although many different formulations exist for simulating nanofluids, the most appropriate for evaluating the impact of volume fraction i.e., percent doping of the base fluid is the Tiwari-Das model [30]. However, this model is restricted since it neglects mass (species) diffusion of the nanoparticles. Buongiorno [31] resolved this issue by formulating a double-diffusive model for nanofluids including thermophoresis and Brownian motion effects, although his model neglects volume fraction. Both approaches have been adopted in many simulations of nanofluid systems. In nanomaterials processing, Sakiadis flows are a key method for producing nano-based coatings. They involve the controlled extrusion of the material over a continuously moving surface and constitute a special type of boundary layer problem. This features in for example nano-slurry machining methods [32], oxalate processing of zirconia- and silica-doped zirconia nano-powders [33] and aluminium oxide metallic nanofluid fabrication via plasma arc deposition on conveying surfaces [34]. In modern oleophobic or superhydrophobic nanocoating processes e.g., NasioITM Sakiadis flows are also utilized [35]. Many diverse studies of nanofluid dynamics from stretching surfaces have been communicated in recent years. Uddin *et al.* [36] used Maple quadrature to compute the g-jitter effects on time-dependent hydromagnetic nanofluid flow from a stretching sheet. Hayat *et al.* [37] employed a non-Fourier thermal relaxation model to study stretching sheet nanofluid flow with variable thickness and conductivity effects. Bhatti *et al.* [38] used a successive linearization algorithm to compute the slip dynamics in magnetic Fe₃O₄-water-based nanofluid flow from a nonlinear stretching sheet adjacent to a permeable material with cross diffusion effects. These studies however neglected rheological effects. Non-Newtonian characteristics of nanofluids have been confirmed at higher volume fractions in many experimental investigations including Maghsoudi *et al.* [39] (for micro-nanostructured polymers deployed in injection molding) and Anil *et al.* [40] (in heat exchangers where rheology of Fe₂O₃, Al₂O₃ and CuO nanoparticles in aqueous carboxymethyl cellulose (CMC) base fluid was studied). Non-Newtonian nanofluid modelling therefore comprises a more robust approach than Newtonian simulation of nanofluids. A number of different models have been used for a variety of complex flows in rheological nanofluid transport phenomena. These include the Stokes' couple stress model [41], Sisko viscoelastic model [42] and Ostwald-deWaele power-law model [43]. Micropolar nanofluid flows have also received some attention. Lund *et al.* [44] studied the heat transfer characteristics in micropolar nanofluid flow from a tilted permeable shrinking/stretching surface with the Buongiorno two-component model. They computed dual solutions for a specific range of shrinking/stretching surface parameters and the mass suction parameter for the opposing flow case. They also showed that skin friction coefficient, heat transfer

coefficient, couple stress coefficient the concentration transfer rate is reduced with increasing micropolar parameter. Gaffar *et al.* [45] used the second order accurate Keller box difference scheme to analyse the flow of micropolar nanofluid from an inverted conical geometry with strong thermal buoyancy forces. Das and Duari [46] simulated the reactive micropolar nanofluid stagnation point flow on a stretching sheet using a Runge–Kutta–Fehlberg integration procedure. Hussanan *et al.* [47] investigated the unsteady free convection flow of micropolar nanofluids from a vertical plate for five types of oxide nanoparticles namely copper oxide, titanium oxide, alumina oxide, iron oxide and graphene oxide suspended in three different types of fluids such as water, kerosene and engine oil. They derived exact solutions using the Laplace transform method and observed that temperature of graphene oxide suspended micropolar nanofluid is higher than other oxide nanoparticles based nanofluids. Prasad *et al.* [48] studied the enrobing thermal convection flow of micropolar nanofluids on a horizontal cylinder using finite difference methods. They observed that micropolar parameter exerts a stronger influence on velocity characteristics whereas Brownian motion and thermophoresis more prominently influence the temperature distributions. Shah *et al.* [49] used an optimal homotopy method to compute the combined effect of magnetic and electric fields on micropolar nanofluid in a rotating channel with Hall current and secondary (cross) flow. Latiff *et al.* [50] studied the time-dependent micropolar nanofluid slip dynamics from an extending/contracting sheet doped with gyrotactic micro-organisms. They observed that skin friction and Nusselt number are reduced whereas microorganism density number is increased with greater values of micropolar parameter, velocity slip, thermal slip and microorganism slip effect.

In modern nanomaterials processing, high temperature conditions are often used [51–53]. These invoke *radiative heat transfer* (e.g., via flame spraying) and this can be used to tune optical properties of manufactured products. In many mathematical studies of nanofluid radiative convection, algebraic flux models are adopted since they circumvent the need for solving the formidable general Integro-differential radiative transfer equation. A popular formulation is the Rosseland diffusion flux model. Pal and Mandal [54] investigated the radiative hydromagnetic micropolar nanofluid transport from a stretching sheet with non-uniform heat source/sink with Runge-Kutta-Fehlberg shooting quadrature. They computed the relative performance of nanoparticle concentration influence on heat and mass transfer characteristics for four types of metallic or non-metallic nanoparticles i.e. silver (Ag), copper (Cu), alumina (Al_2O_3) and titanium dioxide (TiO_2) in aqueous base fluids. Hayat and Khan [55] developed homotopy solutions for radiative convection micropolar nanofluid flow from a stretching sheet with the Buongiorno model, observing that heat and mass transfer rates are elevated for higher values of radiation heat flux and Brownian motion. Kumar *et al.* [56] used the successive linearization method (SLM) to compute the impact of second order slip on electrically conducting mixed convective stagnation point flow of a micropolar Buongiorno nanofluid with thermal radiation, viscous and Joule dissipation, noting that first order slip exerts contrary modifications in fluid velocity and angular velocity (micro-rotation) whereas without second order slip and for strong mixed convection the first order slip induces the opposite response. They also the sheet employed quadratic multiple regression analysis on skin friction coefficient and local Nusselt number distributions, showing that for the case of a free stream with less velocity than stretching velocity, a weak variation in microrotation induces a significant perturbation in skin friction in comparison to the mixed convection parameter. Further studies of radiative micropolar/nanofluid dynamics include Shah *et al.* [57] for gold-water nanofluids and Ferdows *et al.* [58] for generic aqueous nanofluids with spherical nanoparticles.

In the current study, as a simulation of high-temperature nanomaterials processing and manufacturing fluid dynamics for non-Newtonian liquids nanomaterials, the goal of this study is to construct a *nonlinear radiative transport of viscoelastic micropolar nanofluid model*

incorporating non-uniform heat source/sink and chemical reaction across a stretching sheet. Unlike most previous studies, the robust Eringen micro-morphic model in this work correctly simulates the *microstructural (spin)* characteristics of rheological nanomaterials. Other non-Newtonian models (e.g., Maxwell viscoelastic, Bingham plastic etc.) completely ignore microstructural characteristics which are fundamental to their physics. The combined micropolar nanofluid (Eringen and Tiwari-Das models) formulation therefore allows a combined multiphase flow analysis which more accurately represents actual nanoliquids used in for example engineering coating systems. The novelty of the current study is therefore to investigate with a better rheological formulation the boundary layer motion of micropolar nanofluid over a stretching sheet with complex high-temperature industrial effects i.e., non-uniform heat source/sink, thermal radiative flux and chemical reaction. The formulated governing partial differential equations with the combined Eringen micropolar rheological and Tiwari-Das nanoscale model, and the Rosseland diffusion radiative algebraic flux model, are transformed to the system of ordinary differential equations and solved with Runge-Kutta 45 Fehlberg method (Maple **dsolve routine**). Extensive computations are presented for the impact of key rheological, nanoscale and thermophysical parameters and visualized graphically. The computed numerical results are validated with simpler cases from the literature e.g. (Mohapatra *et al.* [59]) to confirm the accuracy of the Maple solutions. The present study will be beneficial to materials processing engineers and provides more realistic simulations of actual nano-liquids using the combined micropolar nanofluid model, compared with existing simpler rheological nanofluid modelling approaches. Furthermore, the Maple solutions also provide a good benchmark for further computational fluid dynamics simulations with commercial software e.g., ANSYS FLUENT, ADINA-F, CFD-ACE etc.

2. MATHEMATICAL NANOMATERIAL FLOW MODEL

Two-dimensional thermo-solutal radiative flow of an incompressible steady aqueous micropolar nanofluid containing spherical nanoparticles from a permeable stretching sheet with non-uniform heat source/sink. The velocity of the stretching sheet is assumed as $U_w = \lambda x$ with $\lambda > 0$ being a constant, where the x and y axes are orientated along the stretching surface and normal to it respectively. The micropolar nanofluid is confined to the region, $y > 0$ (**Figure 1**). It is also assumed that the base fluid and the nanoparticles are in thermal equilibrium and no slip occurs between them. Extending the model in [59] with mass diffusion, heat generation/absorption and first order homogenous chemical reaction effects, the new system of governing equations for the Sakiadis stretching regime can be shown to take the form:

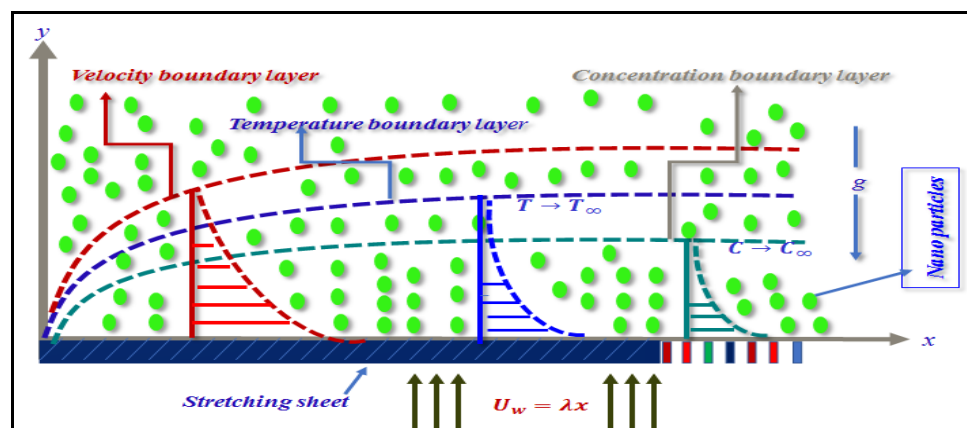


Figure 1: Geometrical model for reactive thermo-solutal micropolar nanofluid Sakiadis flow

$$\frac{\partial u}{\partial x} + \frac{\partial v}{\partial y} = 0 \quad (1)$$

$$u \frac{\partial u}{\partial x} + v \frac{\partial u}{\partial y} = \left(\frac{\mu_{nf} + \kappa}{\rho_{nf}} \right) \frac{\partial^2 u}{\partial y^2} + \frac{\kappa}{\rho_{nf}} \frac{\partial \omega}{\partial y} + g\beta_T (T - T_\infty) + g\beta_c (C - C_\infty) \quad (2)$$

$$u \frac{\partial \omega}{\partial x} + v \frac{\partial \omega}{\partial y} = \left(\frac{\gamma_{nf}}{\rho_{nf} j} \right) \frac{\partial^2 \omega}{\partial y^2} - \frac{\kappa}{\rho_{nf} j} \left(2\omega + \frac{\partial u}{\partial y} \right) \quad (3)$$

$$u \frac{\partial T}{\partial x} + v \frac{\partial T}{\partial y} = \alpha_{nf} \frac{\partial^2 T}{\partial y^2} - \frac{1}{(\rho c_p)_{nf}} \frac{\partial q_{rad}}{\partial y} + \frac{1}{(\rho c_p)_f} q'' \quad (4)$$

$$u \frac{\partial C}{\partial x} + v \frac{\partial C}{\partial y} = D_m \frac{\partial^2 C}{\partial y^2} - K'_r (C - C_\infty) \quad (5)$$

In Eqs. (1)-(5) u and v designate the component of the linear (translation) velocities, ω is microrotational (angular spin) component normal to the xy -plane, κ signifies the Eringen vortex viscosity, j is the micro inertia density, T, T_∞ are fluid and ambient (freestream) temperature and C, C_∞ are fluid and ambient (free stream) concentration. The microelements are assumed no deformable and the stress tensor is symmetric in the Eringen theory for this case. The appropriate boundary conditions imposed are:

$$u = U_w(x) = \lambda cx, v = v_o, \omega = -n \frac{\partial u}{\partial y}, T = T_w, C = C_w \quad \text{at } y = 0 \quad (6)$$

$$u \rightarrow 0, \omega \rightarrow 0, T \rightarrow T_\infty, C \rightarrow C_\infty \quad \text{at } y \rightarrow \infty$$

Further, γ_{nf} is the spin gradient viscosity which is dependent on the nanofluid Newtonian dynamic viscosity (following Brinkman [60]), α_{nf} is thermal diffusivity of nanofluid, ρ_{nf} is the effective density of the nanofluid, $(\rho c_p)_{nf}$ is heat capacitance of the nanofluid (which is known as the Tiwari-Das formulation and is defined following Khanafer *et al.* [61]) and these have the mathematical forms:

$$\begin{aligned} \gamma_{nf} &= \left(\mu_{nf} + \frac{\kappa}{2} \right) j = \mu_f \left(\frac{\mu_{nf}}{\mu_f} + \frac{K}{2} \right) j, \quad K = \frac{\kappa}{\mu_f}, \quad \alpha_{nf} = \frac{k_{nf}}{(\rho c_p)_{nf}}, \\ \rho_{nf} &= (1-\phi)\rho_f + \phi\rho_s = \rho_f \left[(1-\phi) + \frac{\rho_s}{\rho_f} \right], \quad \mu_{nf} = \frac{\mu_f}{(1-\phi)^{2.5}}, \\ (\rho c_p)_{nf} &= (1-\phi)(\rho c_p)_f + \phi(\rho c_p)_s, \quad k_{nf} = k_f \left[\frac{(k_s + 2k_f) - 2\phi(k_f - k_s)}{(k_s + 2k_f) + \phi(k_f - k_s)} \right]. \end{aligned} \quad (7)$$

Furthermore, following [62], the thermophysical properties of the base fluid (water) and different metallic nanoparticles (gold, silver, copper) materials are given in **Table 1**.

Table 1. Thermo-physical properties of water and different nanoparticles

Material	Symbol	ρ ($kg\ m^{-3}$)	Cp ($J\ kg^{-1}K^{-1}$)	κ ($Wm^{-1}K^{-1}$)
Pure water	H ₂ O	997.1	4179	0.6130
Silver	Ag	10500	235	429
Gold	Au	19300	129	318
Copper	Cu	8933	385	401

The net radiative heat flux, which is unidirectional, following [55]-[59] is expressed as:

$$q_{rad} = -\frac{4\sigma^*}{3k^*} \frac{\partial T^4}{\partial y} = -\frac{16\sigma^*}{3k^*} \frac{\partial}{\partial y} \left(T^3 \frac{\partial T}{\partial y} \right) \quad (8)$$

Where σ^* is Stefan-Boltzmann constant and k^* is Rosseland spectral absorption coefficient. Further, the non-uniform heat source/sink q''' is adopted following Pal and Chatterjee [63] as:

$$q''' = \frac{k_{nf} U_w(x)}{x \nu_f} \left[A^* (T_w - T_\infty) f'(\eta) + B^* (T - T_\infty) \right] \quad (9)$$

Where A^* and B^* are parameters of the space-dependent and temperature-dependent internal heat generation/absorption respectively. $A^*, B^* > 0$ represents *heat generation* and $A^*, B^* < 0$ represents *heat absorption*. We define θ and ϕ i.e., the dimensionless temperature and nanoparticle volume fraction (concentration) of the nanofluids as $\theta = (T - T_\infty) / (T_w - T_\infty)$ and $\phi = (C - C_\infty) / (C_w - C_\infty)$. The quartic temperature term, T^4 appearing in equation (8) may then be expressed as:

$$T^4 \cong T_\infty^4 \{1 + (\theta_w - 1)\theta\}^4, \quad \theta_w = T_w / T_\infty \quad (10)$$

Equations (1)-(7) admit self-similar solutions of the following form:

$$\psi(x, y) = \sqrt{c \nu_f} x f(\eta), \quad \omega(x, y) = c \sqrt{\frac{c}{\nu_f}} x g(\eta), \quad \eta = y \sqrt{\frac{c}{\nu_f}} \quad (11)$$

Where ν_f is the kinematic viscosity of the nanofluid, C is constant and ψ is stream function

which is defined via the Cauchy-Riemann equations, $u = \frac{\partial \psi}{\partial y}$ and $v = -\frac{\partial \psi}{\partial x}$, then we have:

$$u = c x f'(\eta), \quad v = -\sqrt{c \nu_f} f(\eta) \quad (12)$$

Using (7) - (12) into equations (2)-(6), we have the self-similar boundary layer equations:

$$\frac{(L_1 + K)}{L_2} f''' + f f'' - (f')^2 + \frac{K}{L_2} g' + Gr \theta + Gm \phi = 0 \quad (13)$$

$$\frac{(L_1 + (K/2))}{L_2} g'' + f g' - f' g - \frac{K}{L_2} (2g + f'') = 0 \quad (14)$$

$$\frac{1}{Pr} \left[\left(\left\{ \frac{k_{nf}}{k_f} + R \{1 + (\theta_w - 1)\theta\}^3 \right\} \theta' \right)' + (A^* f' + B^* \theta) \right] + L_3 f \theta' = 0 \quad (15)$$

$$\phi'' + Sc f \phi' - Sc Kc \phi = 0 \quad (16)$$

The transformed boundary conditions emerge as:

$$\begin{aligned} f(0) = S, \quad f'(0) = \lambda, \quad g(0) = -n f''(0), \quad \theta(0) = 1, \quad \phi(0) = 1 \\ f'(\infty) = 0, \quad g(\infty) = 0, \quad \theta(\infty) = 0, \quad \phi(\infty) = 0 \end{aligned} \quad (17)$$

The non-dimensional parameters featured in Eqs. (13)- (17) are the Eringen micropolar material parameter K , modified thermal Grashof number Gr , modified solutal (nanoparticle) Grashof number Gm , Prandtl number Pr , radiation-conduction parameter R , Schmidt number Sc , first-order chemical reaction parameter Kc and wall suction parameter S which are defined as follows:

$$K = \frac{\kappa}{\mu_f}, Gr = \frac{g\beta_T(T-T_\infty)}{c^2 x}, Gm = \frac{g\beta_c(C-C_\infty)}{c^2 x}, Pr = \frac{\nu_f}{\alpha_f} \quad (18)$$

$$R = -\frac{16\sigma^*T_\infty^3}{3k_f k^*}, Sc = \frac{\nu_f}{D_m}, Kc = \frac{K'r}{c}, S = -\frac{v_0}{\sqrt{c\nu_f}}$$

Also, the following volume fraction algebraic expressions arising in Eqs. (13)-(15) are defined as:

$$L_1 = (1-\phi)^{-2.5}, L_2 = 1-\phi + \phi \frac{\rho_s}{\rho_f}, L_3 = 1-\phi + \phi \frac{(\rho c_p)_s}{(\rho c_p)_f} \quad (19)$$

Key physical quantities of relevance to sheet nanomaterials processing are the wall gradients of the primitive transport variables (velocity, micro-rotation, temperature and nanoparticle concentration). These are respectively the *skin friction coefficient*, *couple stress coefficient*, *Nusselt number* and *Sherwood number* which may be estimated by the following expressions

$$C_f = \frac{\tau_w}{\rho_{nf} U_w^2}, \quad \text{where } \tau_w = \left[(\mu_{nf} + \kappa) \frac{\partial u}{\partial y} + \kappa \omega \right]_{y=0} \quad (20)$$

$$C_w = \frac{x}{c} \left[\frac{\partial \omega}{\partial y} \right]_{y=0} \quad (21)$$

$$Nu_x = \frac{x q_w}{k_{nf} (T_w - T_\infty)}, \quad \text{where } q_w = k_{nf} \left(-\frac{\partial T}{\partial y} \right)_{y=0} - \frac{4\sigma^*}{3k^*} \left(-\frac{\partial T^4}{\partial y} \right)_{y=0} \quad (22)$$

$$Sh_x = \frac{x q_m}{D_m (C_w - C_\infty)}, \quad \text{where } q_m = D_m \left[\frac{\partial C}{\partial y} \right]_{y=0} \quad (23)$$

Here τ_w (surface shear stress), q_w (surface heat flux) and q_m (surface mass flux). Now the dimensionless forms of skin friction coefficient, couple stress coefficient, Nusselt number and Sherwood number emerge as:

$$C_f = \frac{L_1 + (1-n)K}{L_2 \sqrt{Re_x}} f''(0), \quad (24)$$

$$C_w = \sqrt{Re_x} g'(0), \quad (25)$$

$$Nu_x = -(1+R\theta_w^3) \sqrt{Re_x} \theta'(0), \quad (26)$$

$$Sh_x = -\sqrt{Re_x} \phi'(0) \quad (27)$$

Here $Re_x = U_w(x) x / \nu_f$ is the *local Reynolds number* based on the sheet stretching velocity.

3. MAPLE NUMERICAL SHOOTING METHOD

The transformed coupled, nonlinear ordinary differential equations (13)-(16) subject to the boundary conditions are solved numerically by using Maple *dsolve routine*. The system of equations is of the parabolic type and it can be solved by several numeric techniques (common finite difference method with central differencing) such as Runge-Kutta-Fehlberg method or Shooting method. In the system of equations, the boundary conditions are specified at the two

ends of the interval. This type of problem is known as a two-point boundary value problem. The default method used for solving initial value problems (IVP) in Maple is a Runge-Kutta-Fehlberg method. However, *dsolve* replaces the boundary value problem (BVP) with an initial value problem (IVP). One way to guarantee accuracy in the solution of an IVP is to solve the problem twice using step sizes h and $h/2$, compare answers at the mesh points corresponding to the larger step size. However, this requires a significant amount of computation for the smaller step size and must be repeated if it is determined that the agreement is not good enough. The Runge-Kutta-Fehlberg method (denoted RKF45) is one way to try to resolve this problem. It features a robust procedure to determine if the proper step size h is being used. At each step, two different approximations for the solution are made and compared. If the two answers are in close agreement, the approximation is accepted. If the two answers do not agree to a specified accuracy, the step size is reduced. If the answers agree to more significant digits than required, the step size is increased. Each step requires the use of the following six values:

$$k_1 = h f(t_k, y_k), \quad (28)$$

$$k_2 = h f\left(t_k + \frac{h}{4}, y_k + \frac{k_1}{4}\right), \quad (29)$$

$$k_3 = h f\left(t_k + \frac{3}{8}h, y_k + \frac{3}{32}k_1 + \frac{9}{32}k_2\right), \quad (30)$$

$$k_4 = h f\left(t_k + \frac{12}{13}h, y_k + \frac{1932}{2197}k_1 - \frac{7200}{2197}k_2 + \frac{7296}{32}k_3\right), \quad (31)$$

$$k_5 = h f\left(t_k + h, y_k + \frac{439}{216}k_1 - 8k_2 + \frac{3680}{513}k_3 - \frac{845}{4104}k_4\right), \quad (32)$$

$$k_6 = h f\left(t_k + \frac{1}{2}h, y_k - \frac{8}{27}k_1 + 2k_2 - \frac{3544}{2565}k_3 + \frac{1859}{4104}k_4 - \frac{11}{40}k_5\right) \quad (33)$$

Then an approximation to the solution of the IVP is made using a Runge-Kutta method of order 4:

$$y_{k+1} = y_k + \left(\frac{25}{216}k_1 + \frac{1408}{2565}k_3 + \frac{2197}{4104}k_4 - \frac{1}{5}k_5\right) \quad (34)$$

A better value for the solution is determined using a Runge-Kutta method of order 5:

$$y_{k+1} = y_k + \left(\frac{16}{135}k_1 + \frac{6656}{12825}k_3 + \frac{28561}{56430}k_4 - \frac{9}{50}k_5 + \frac{2}{55}k_6\right) \quad (35)$$

Further details are provided in Bég et al. [64].

4. VALIDATION WITH PUBLISHED STUDIES

To benchmark the validity of the present MAPLE solutions, a comparison is made with the Adomian decomposition solutions for the earlier model of Mahopatra *et al.* [59]. When *mass diffusion* is neglected in the present model (i.e. Eqn. (16) vanishes), and with $Gm, Gc = 0$ (thermal and species buoyancy vanish- in [59] this corresponds to the default solution of $\lambda_1 = 0$ i.e., thermal buoyancy parameter vanishing), $A^*, B^* = 0$ absence of *heat generation or absorption*) and neglecting nanoparticle concentration boundary conditions, the present model contracts to exactly the radiative micropolar nanofluid Sakiadis model of Mahopatra *et al.* [59]:

$$\frac{(L_1 + K)}{L_2} f''' + f f'' - (f')^2 + \frac{K}{L_2} g' = 0 \quad (38)$$

$$\frac{(L_1 + (K/2))}{L_2} g'' + f g' - f' g - \frac{K}{L_2} (2g + f'') = 0 \quad (37)$$

$$\frac{1}{\text{Pr}} \left\{ \frac{k_{nf}}{k_f} + R \{1 + (\theta_w - 1)\theta\}^3 \theta' \right\} + L_3 f \theta' = 0 \quad (38)$$

$$f(0) = S, \quad f'(0) = \lambda, \quad g(0) = -nf''(0), \quad \theta(0) = 1, \quad (38)$$

$$f'(\infty) = 0, \quad g(\infty) = 0, \quad \theta(\infty) = 0$$

The comparison solutions are shown in **Table 1**. Excellent agreement is obtained. These solutions also concur very closely with earlier computations by Fauzi *et al.* [65]. Table 1 shows that increasing nanoparticle volume fraction, φ , increases skin friction magnitudes for both micropolar nanofluids ($K > 0$) and Newtonian nanofluids ($K = 0$); however the impact is more prominent in the latter. This implies that greater deceleration is induced for Newtonian fluids compared with micropolar nanofluids and this confirms the drag reducing properties of micropolar fluids [66]. Micro-rotation gradient i.e. wall couple stress magnitudes are also enhanced with increasing nanoparticle volume fraction and in particular with greater Eringen micropolar parameter, K . Finally Nusselt number function (wall heat transfer rate) magnitudes are strongly decreased with greater volume fraction and also micropolar parameter. The former confirms the heat enhancement in the boundary layer (heat is convected away from the wall to the micropolar nanofluid so that heat transfer to the wall is reduced). The latter indicates that micropolarity in the fluid cools the boundary and heats the main body of the flow.

Table 1: Comparison of skin friction, couple stress and Nusselt number function for nanoparticle volume fraction and Eringen micropolar parameters and Cu-Water nanofluid

φ	K	$f''(0)$	$g'(0)$	$\theta'(0)$	$f''(0)$	$g'(0)$	$\theta'(0)$
		Present (MAPLE)			Mahopatra <i>et al.</i> [59]		
0	0	-0.998	-0.0249	-1.34361	-0.101	-0.0255	-1.34382
0	1	-0.08144	-0.01599	-1.35957	-0.08203	-0.01608	-1.35948
0.1	0	-0.11995	-0.0358	-0.97234	-0.12034	-0.0362	-0.97229
0.1	1	-0.10104	-0.02492	-0.98881	-0.10096	-0.02498	-0.98874
0.2	0	-0.12514	-0.03941	-0.69012	-0.12527	-0.03923	-0.69003
0.2	1	-0.10897	-0.02944	-0.7041	-0.10916	-0.02938	-0.7037

5. RESULTS AND DISCUSSION

Extensive MAPLE numerical solutions are illustrated in **Figs. 2-29**. All default parameter values are given in the legends.

Figs. 2-5 visualize the linear velocity, temperature, angular velocity (micro-rotation) and nanoparticle concentration distributions with various thermal Grashof number (Gr) and wall suction (S) parameter values, The default parameter values correspond to highly aqueous nanoparticles [67] (where thermal diffusion and momentum diffusion are approximately equal i.e.

$Pr = 1$), $K = 0.2$ (weak micropolar behavior), $Gm = 2$ (nanoparticle species buoyancy force is double the viscous hydrodynamic force), $R = 0.5$ (thermal conduction dominates thermal radiation), $A_1 = B_1 = 0.1$ (space-dependent and temperature-dependent internal heat generation due to a “hot spot” [68]), $Sc = 0.6$ (nanoparticle mass diffusion exceeds momentum diffusion), $Kc = 0.5$ (weak homogenous destructive reaction), $S > 0$ (wall suction) and $n = 0.5$ (weak concentrations of microelements at the wall, see Peddieson and McNitt [69]).

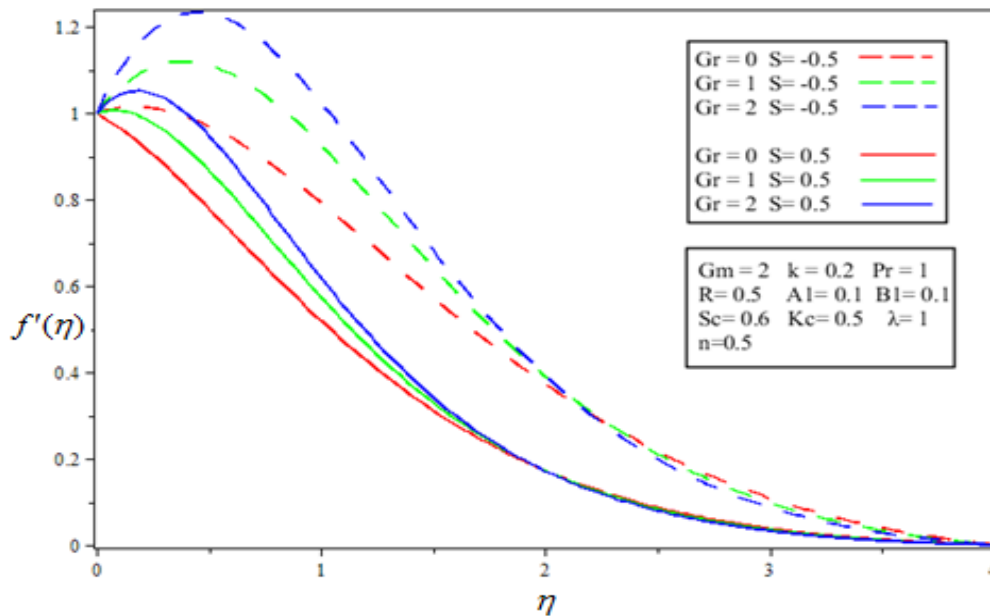


Figure 2: Velocity profiles for Gr and S variation

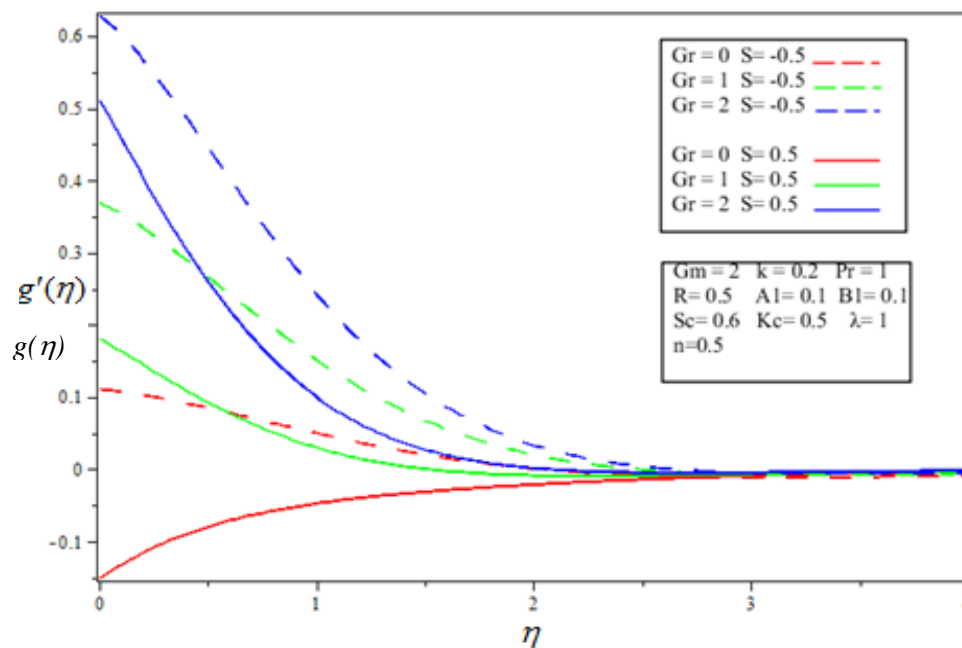


Figure 3: Microrotation profiles for Gr and S variation

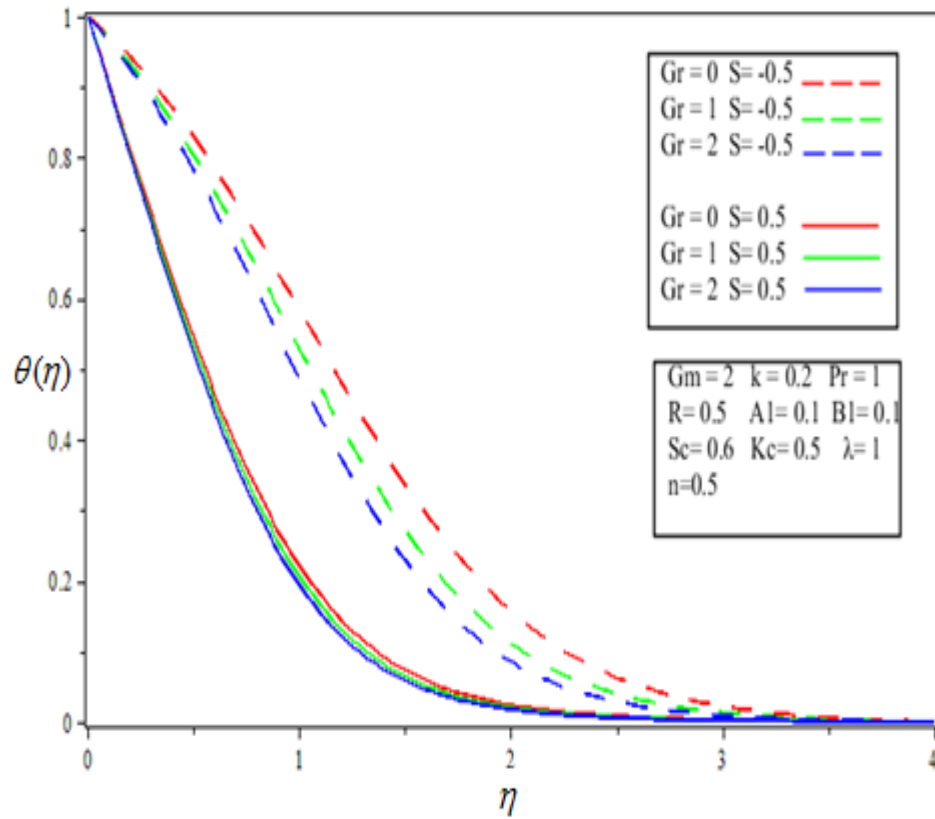


Figure 4: Temperature profiles for Gr and S variation

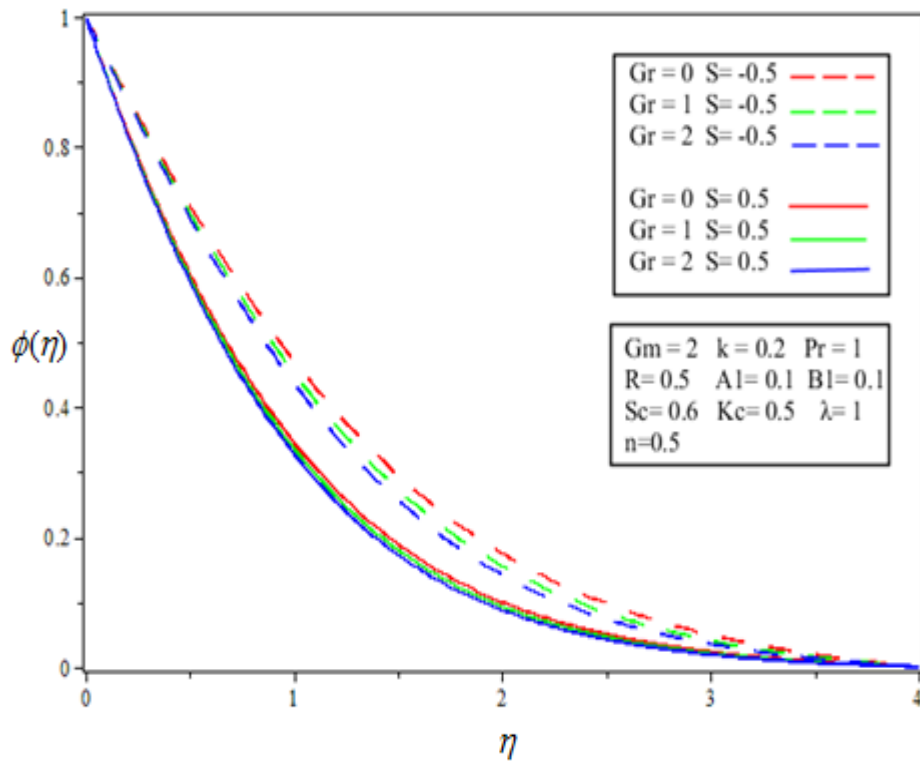


Figure 5: Nanoparticle concentration profiles for Gr and S variation

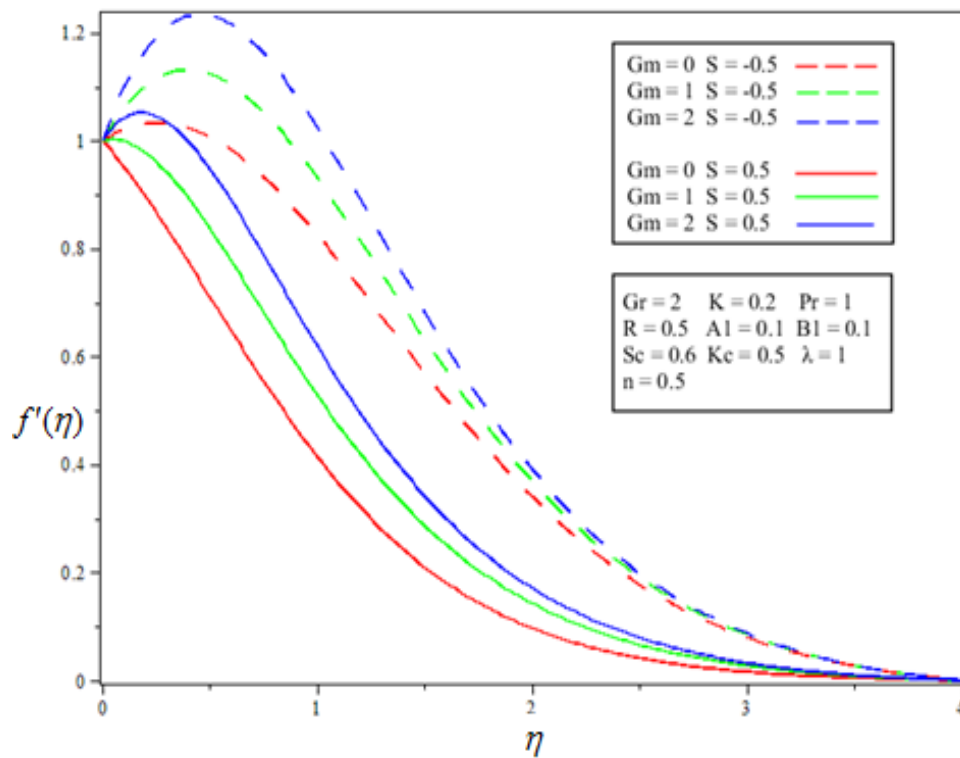


Figure 6: Velocity profiles for Gm and S variation

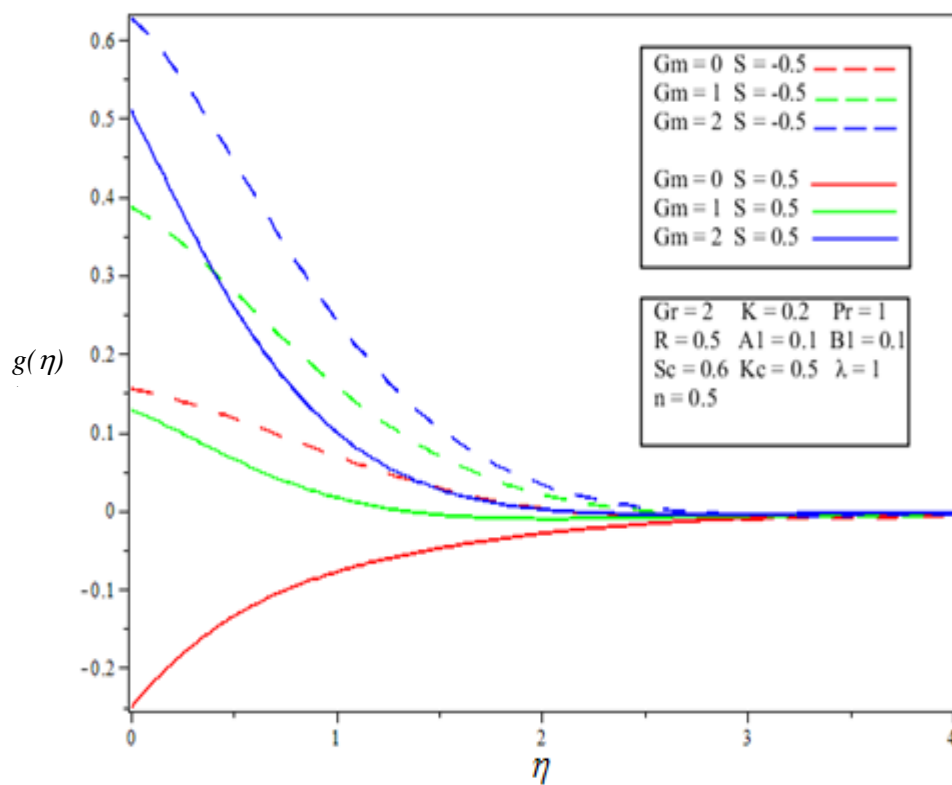


Figure 7: Microrotation profiles for Gm and S variation

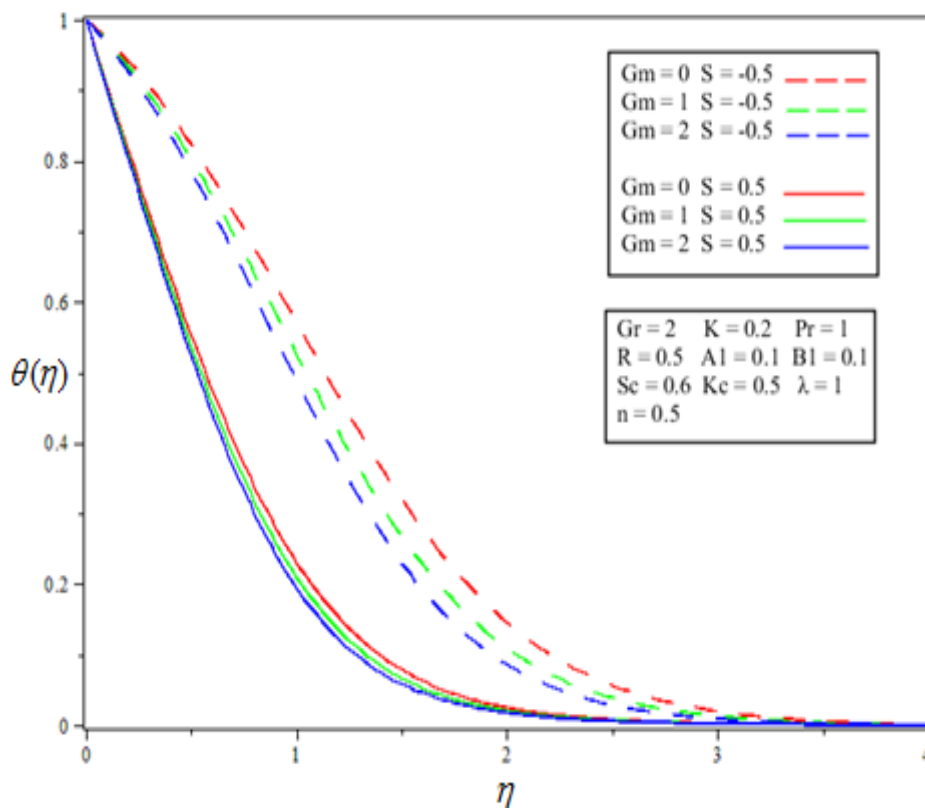


Figure 8: Temperature profiles for Gm and S variation

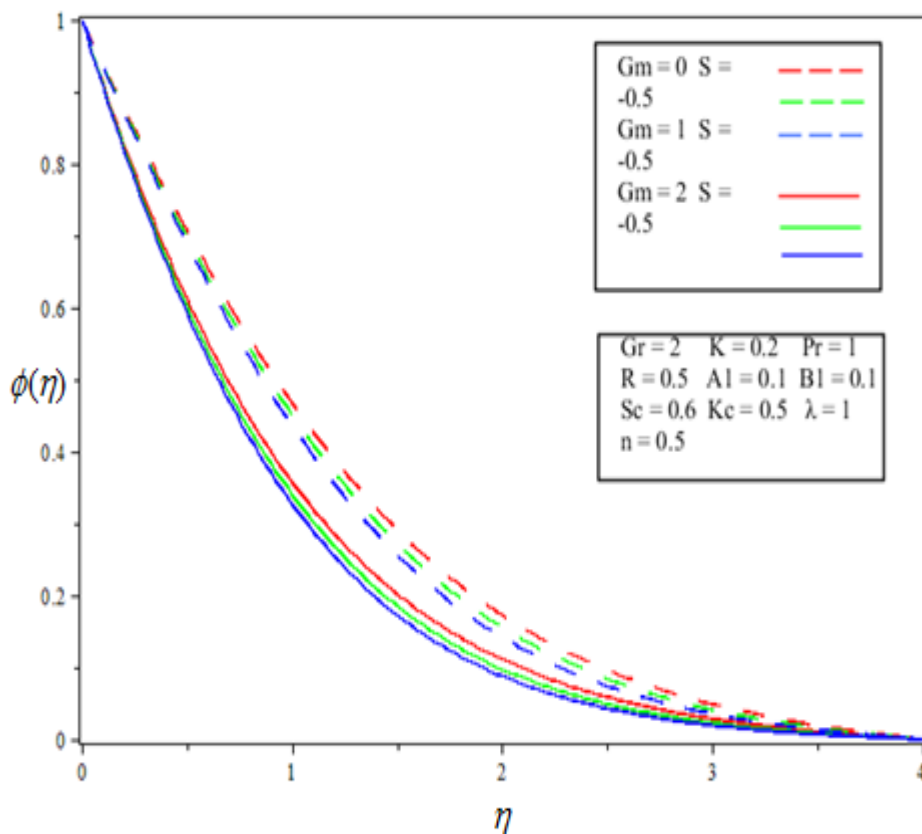


Figure 9: Nanoparticle concentration profiles for Gm and S variation

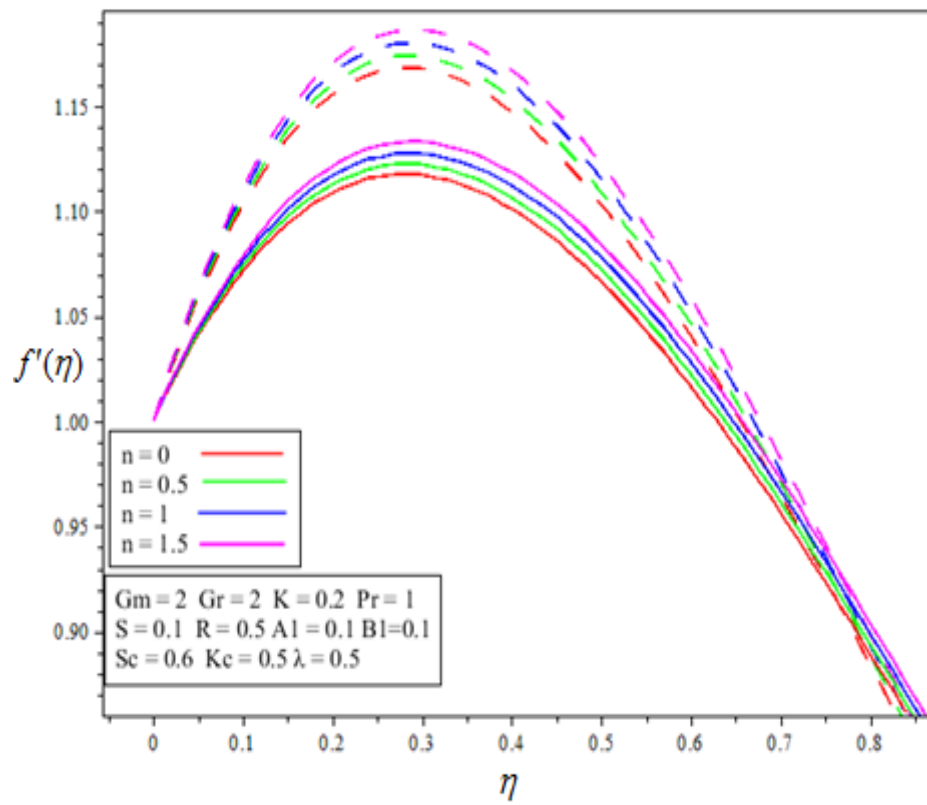


Figure 10: Velocity profiles for n variation

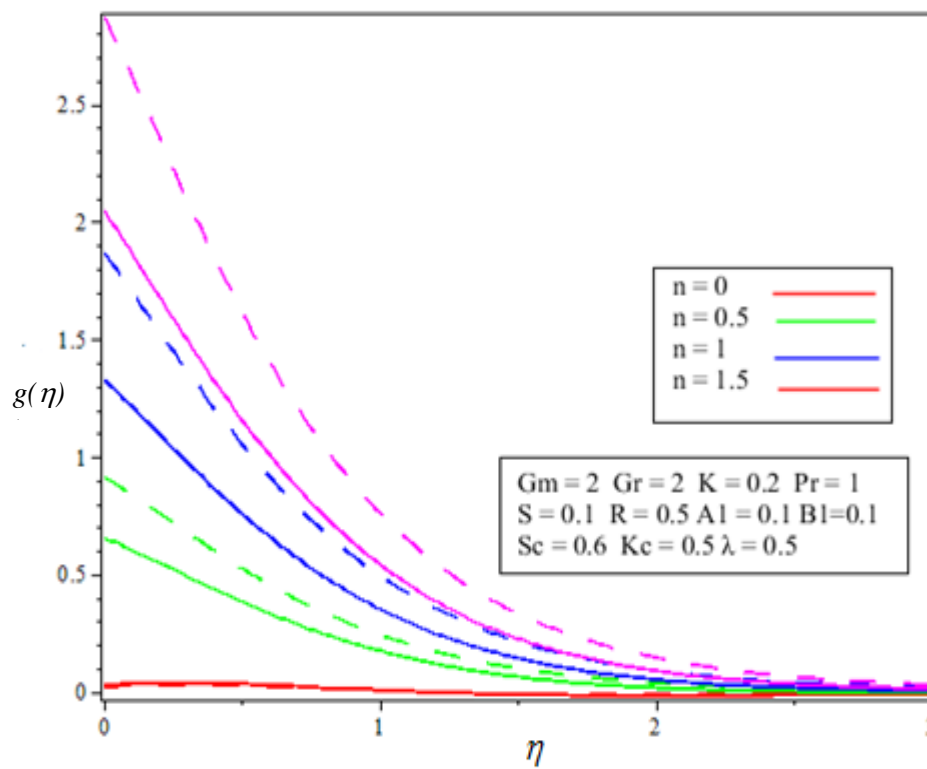


Figure 11: Microrotation profiles for n variation

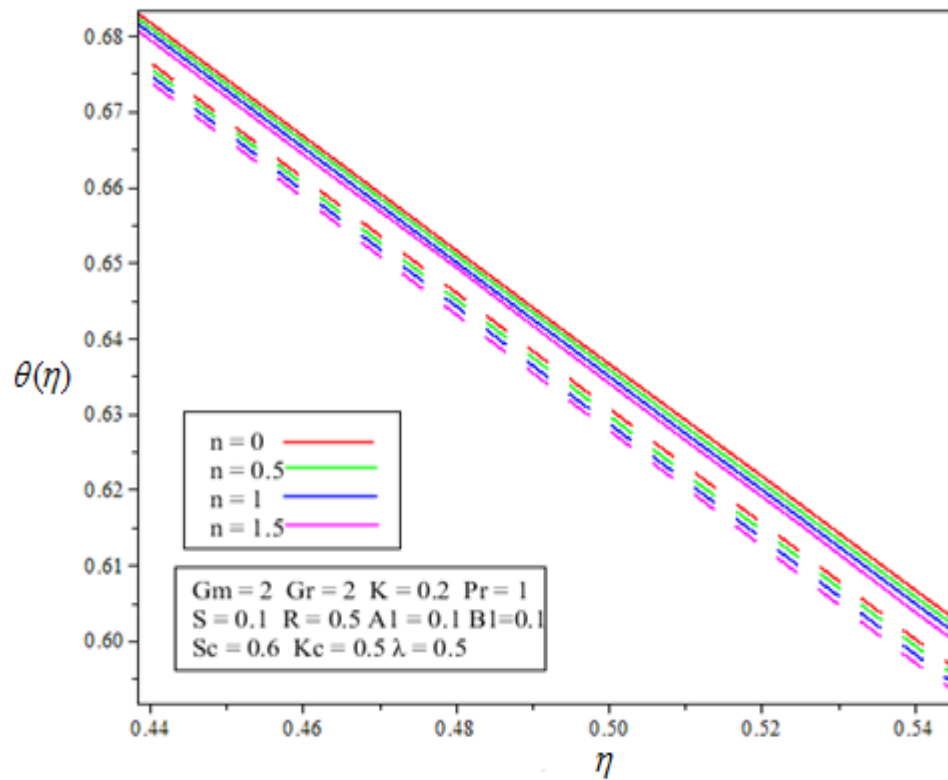


Figure 12: Temperature profiles for n variation

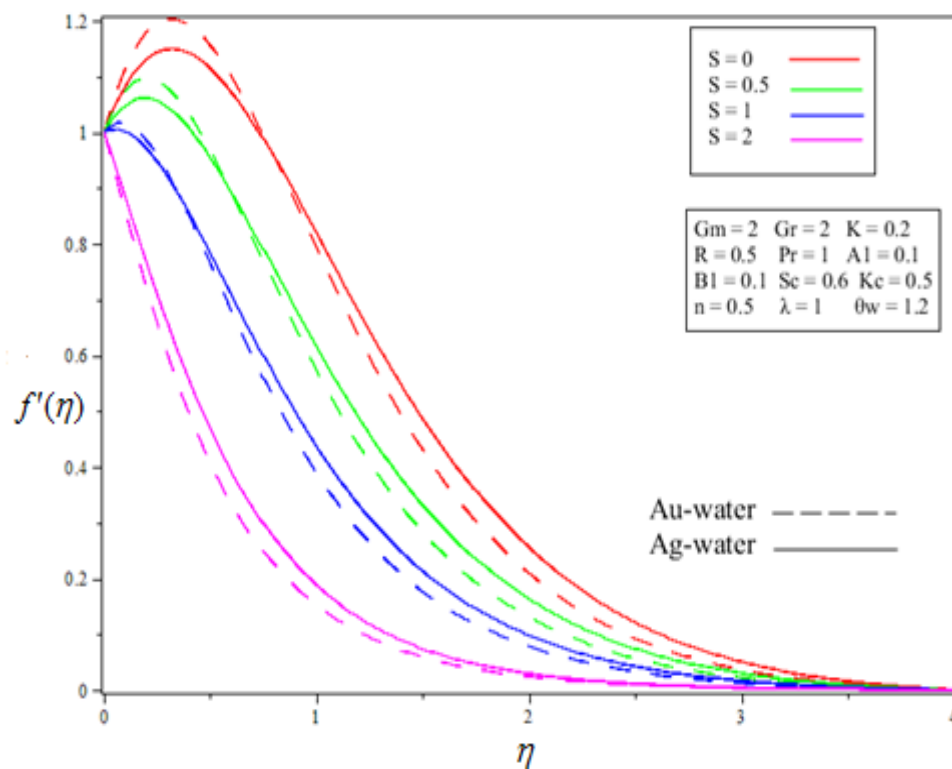


Figure 13: Velocity profiles for S variation and silver versus gold nanoparticles

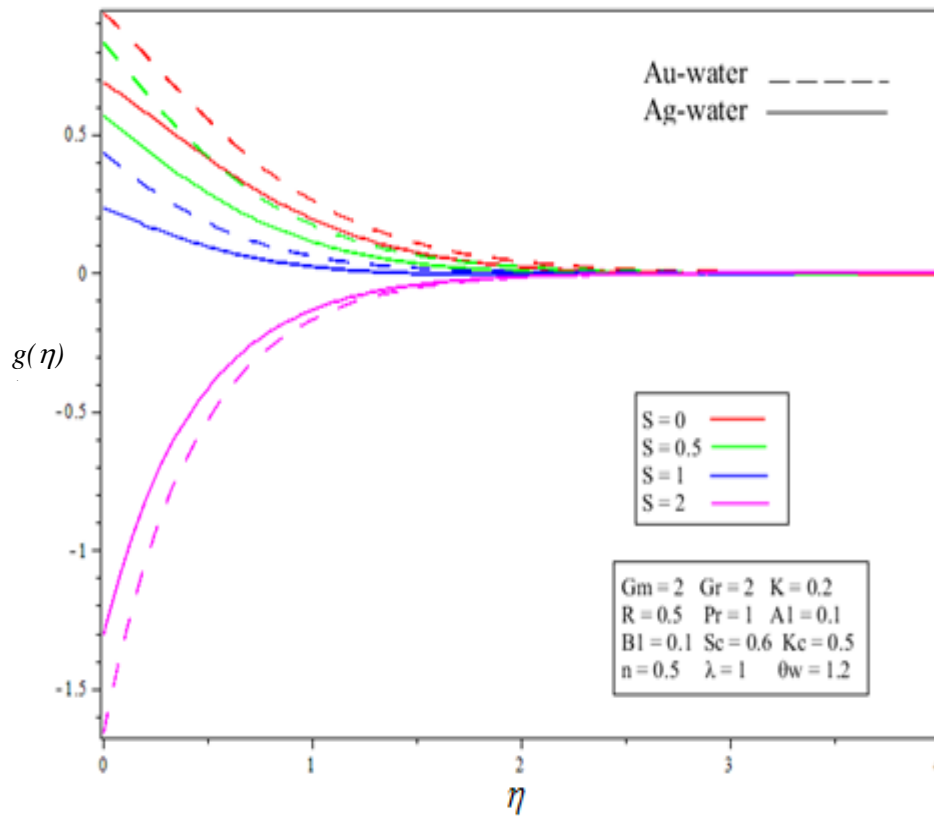


Figure 14: Microrotation profiles for S variation and silver versus gold nanoparticles

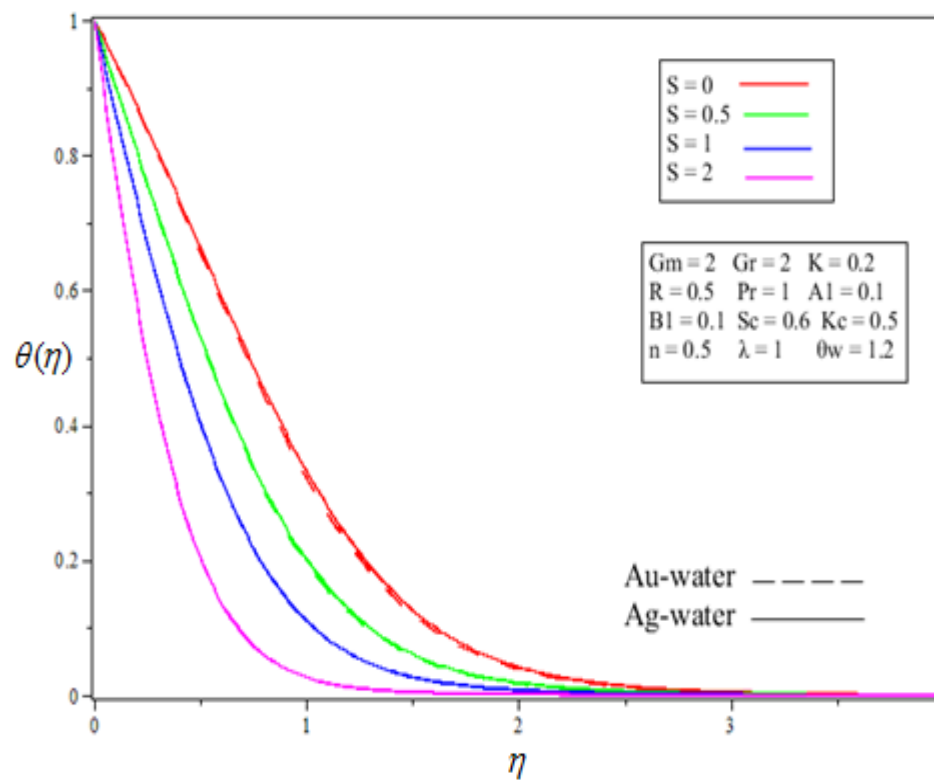


Figure 15: Temperature profiles for S variation and silver versus gold nanoparticles

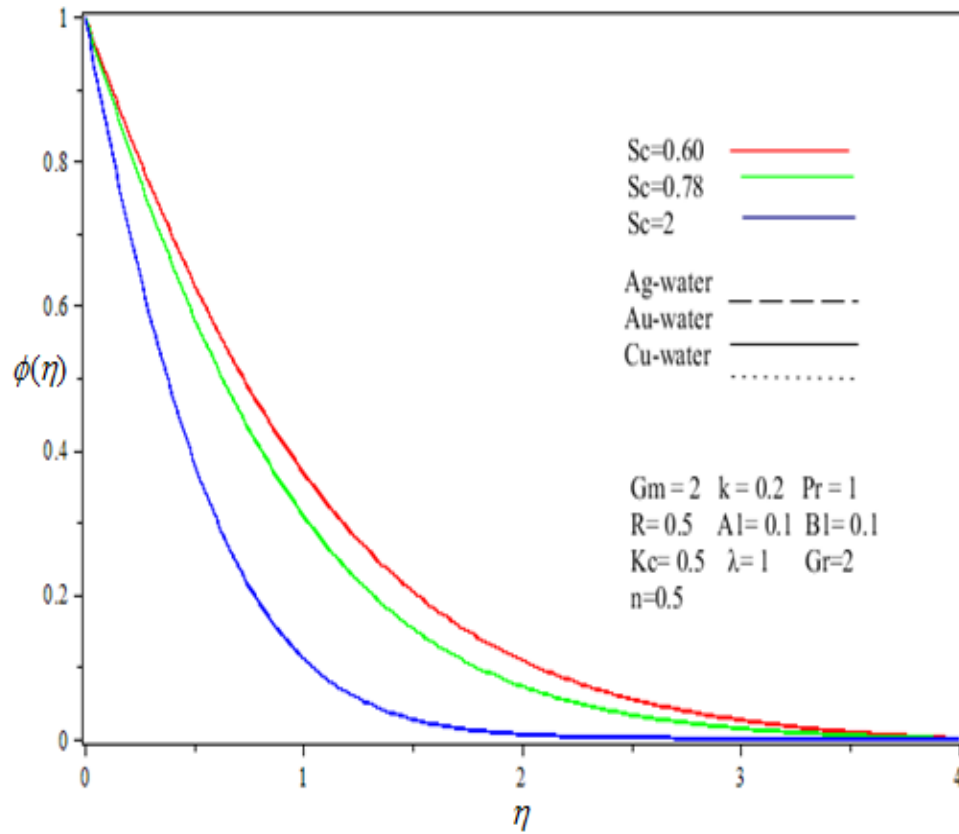


Figure 16: Nanoparticle concentration profiles for Sc variation and silver versus gold nanoparticles

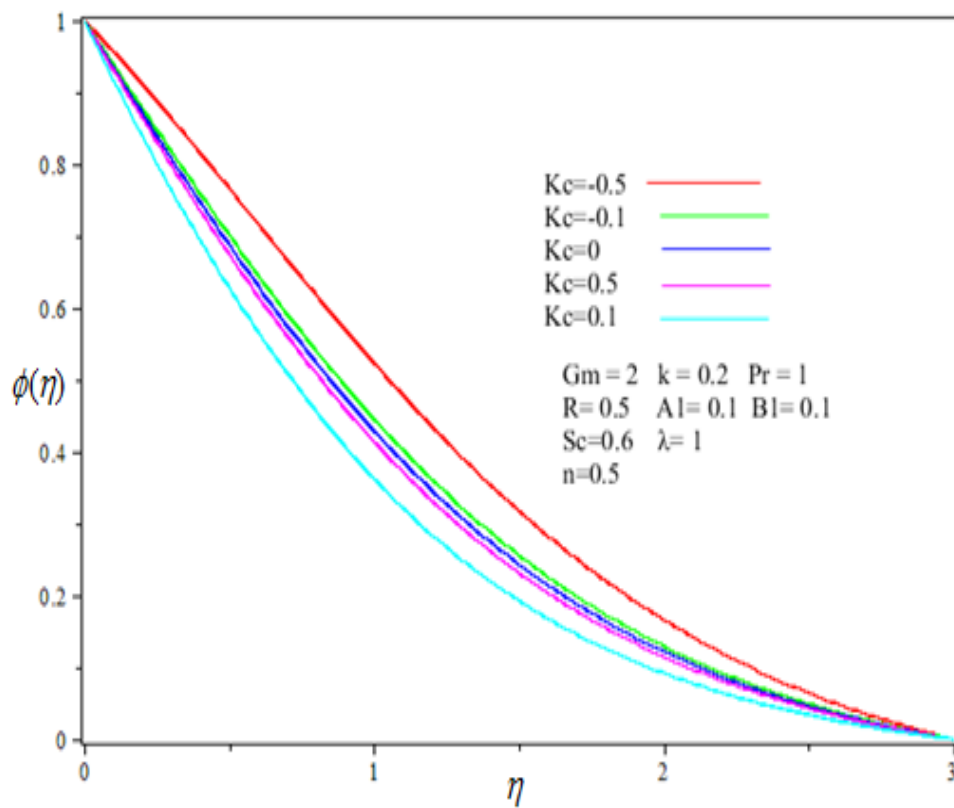


Figure 17: Nanoparticle concentration profiles for Kc variation

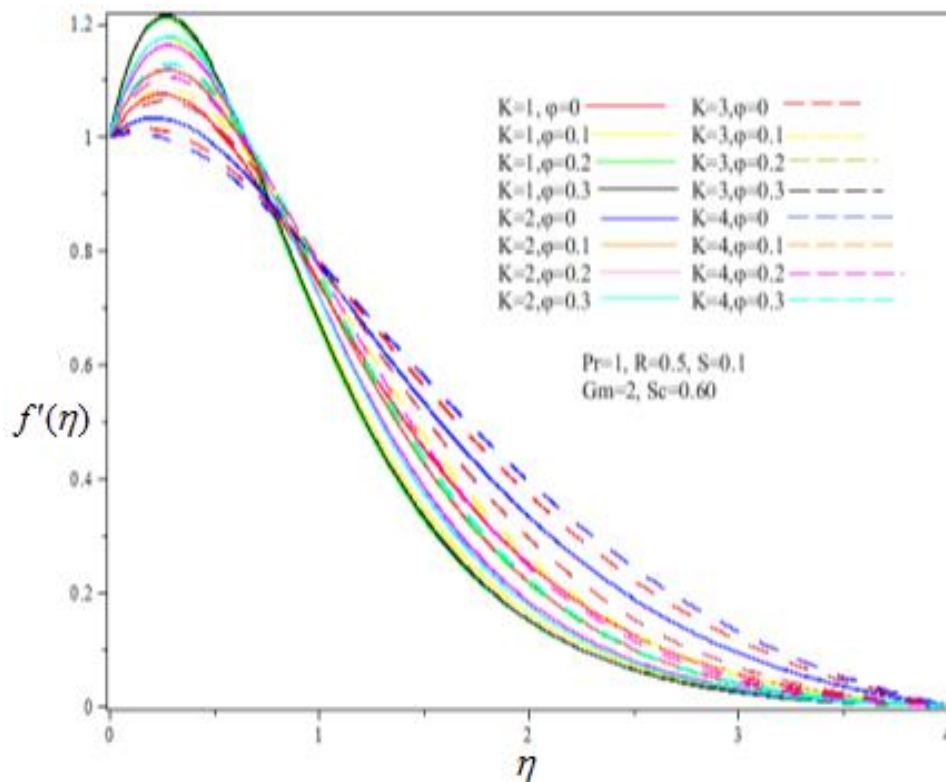


Figure 18: Velocity profiles for various K and φ (Au-Water)

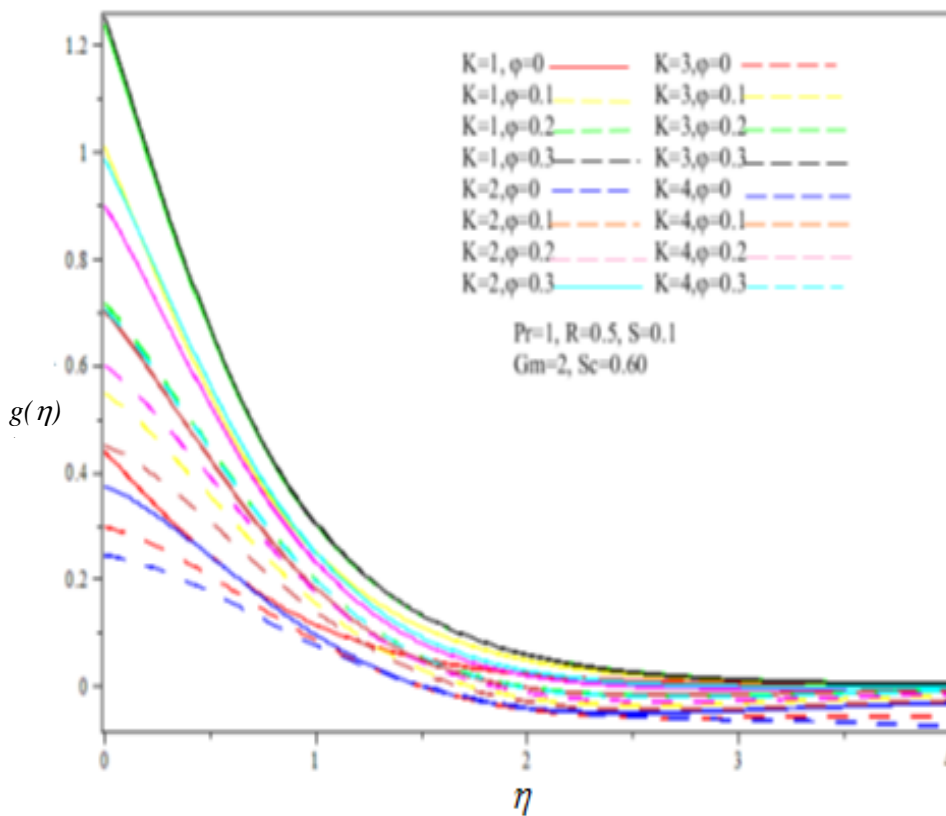


Figure 19: Microrotation profiles for various K and φ (Au-Water)

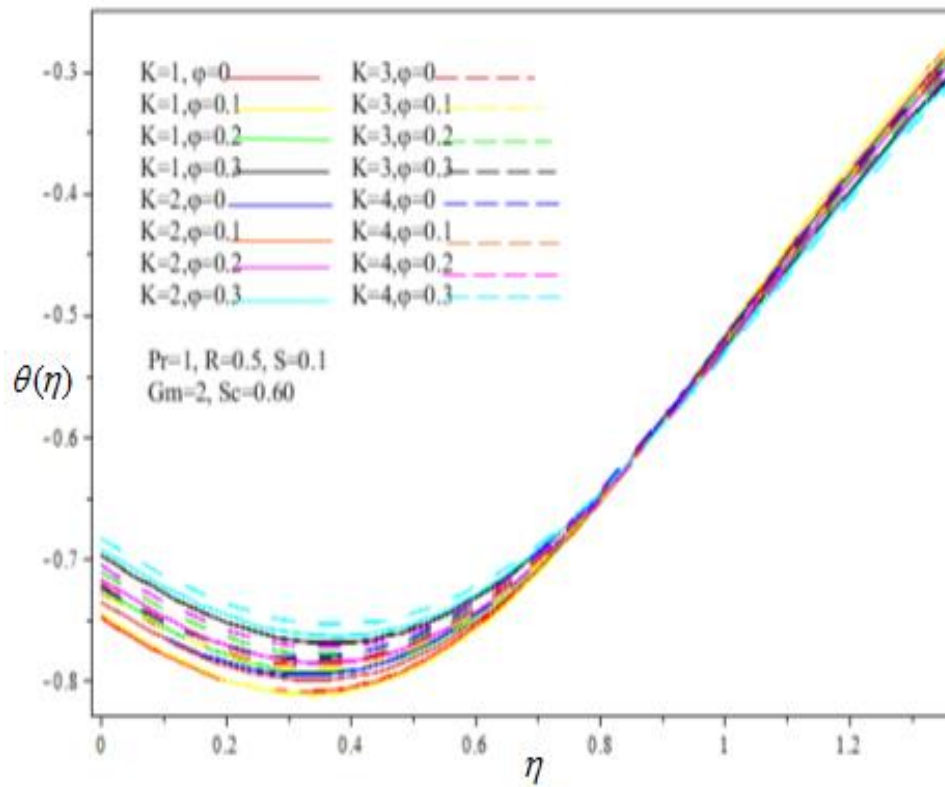


Figure 20: Temperature profiles for various K and φ (Au-Water)

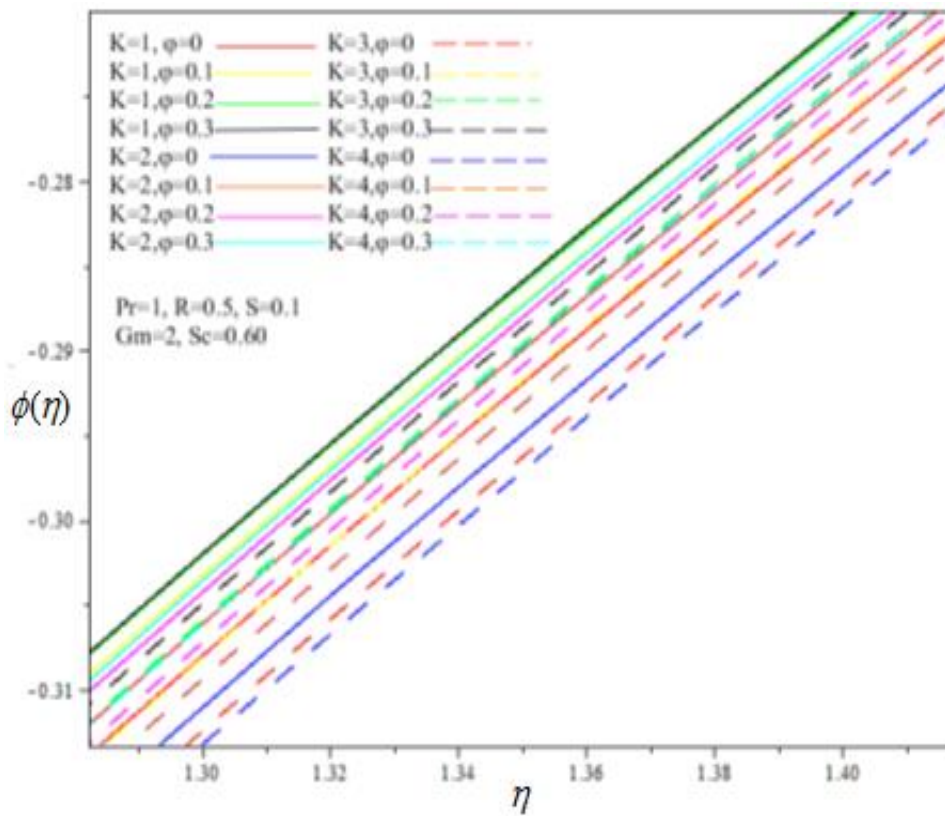


Figure 21: Nanoparticle concentration profiles for various K and φ (Au-Water)

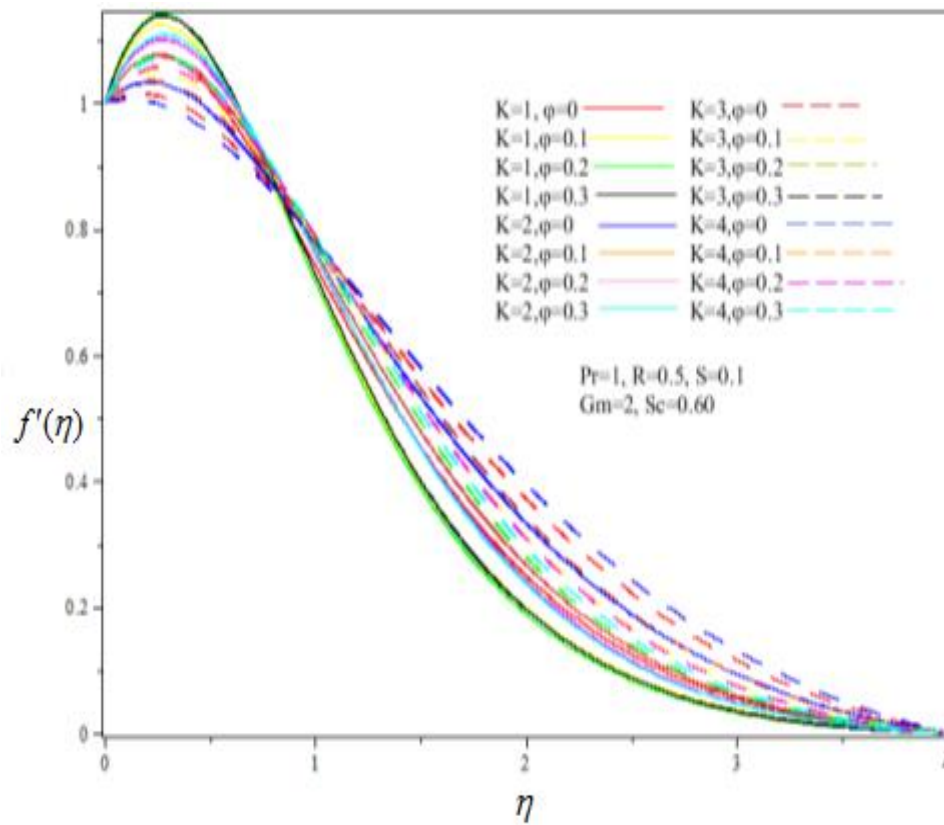


Figure 22: Velocity profiles for various K and φ (Ag-Water)

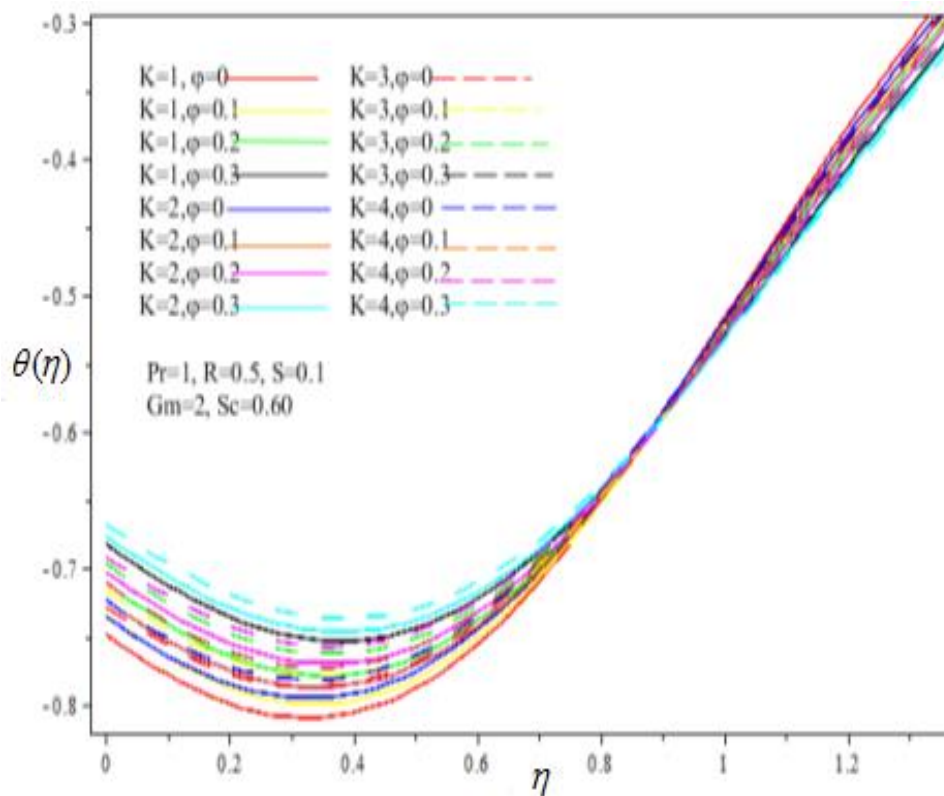


Figure 23: Temperature profiles for various K and φ (Ag-Water)

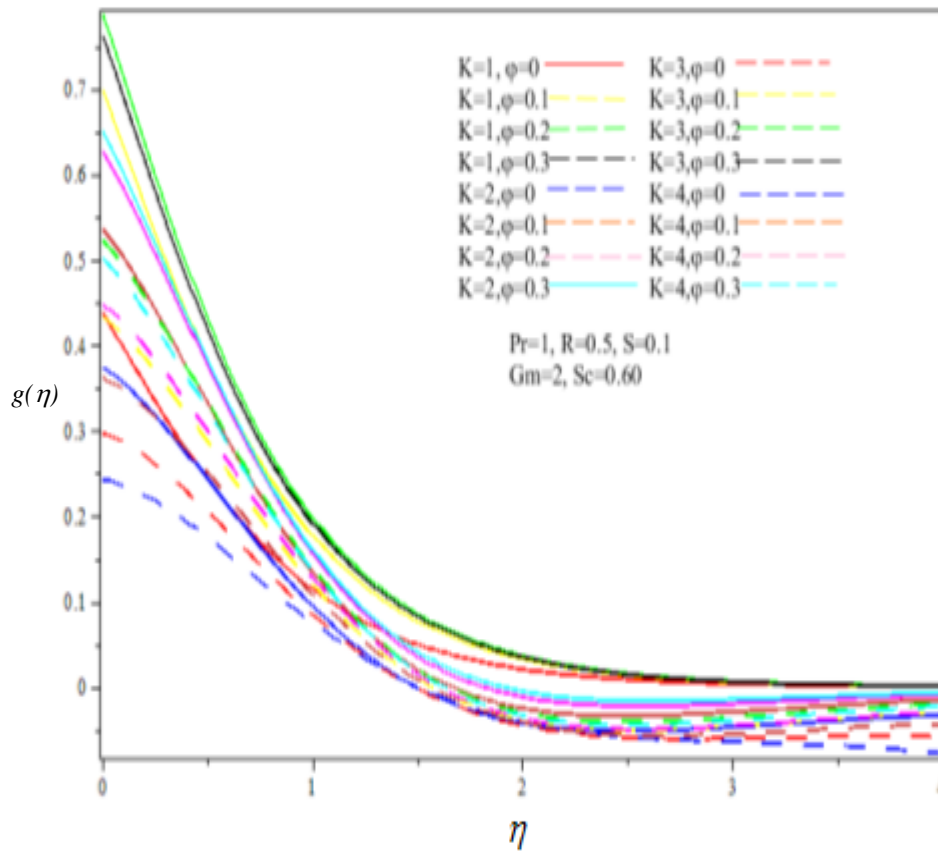


Figure 24: Microrotation profiles for various K and ϕ (Ag-Water)

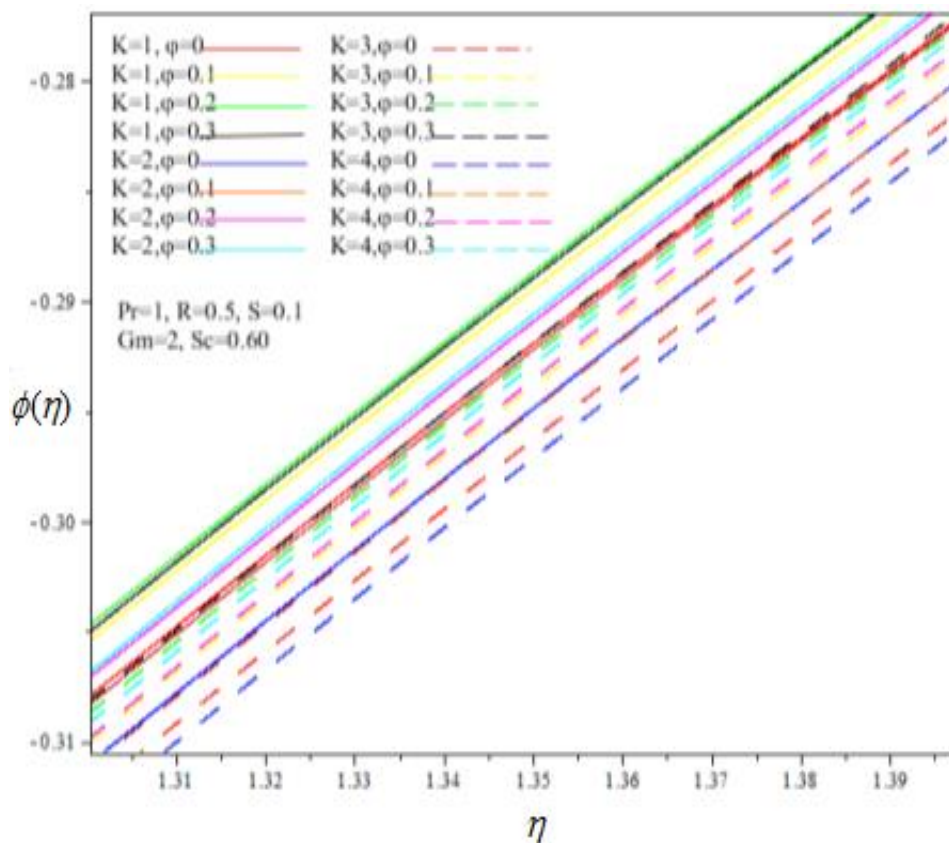


Figure 25: Nanoparticle concentration profiles for various K and ϕ (Ag-Water)

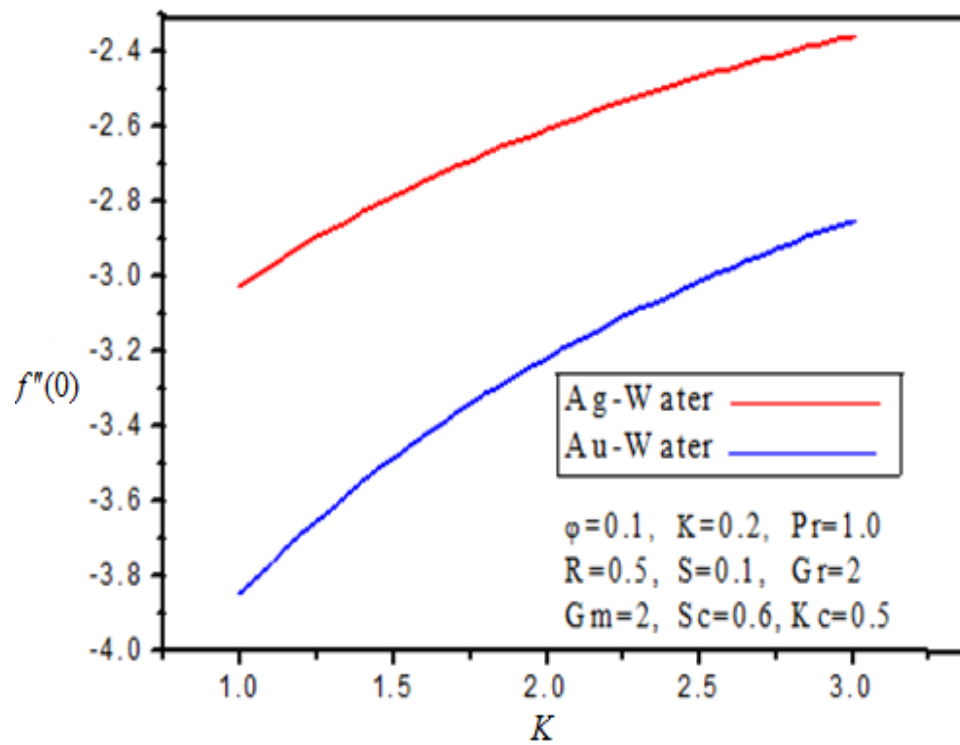


Figure 26: Effect of K on skin friction for silver and gold water nanofluids

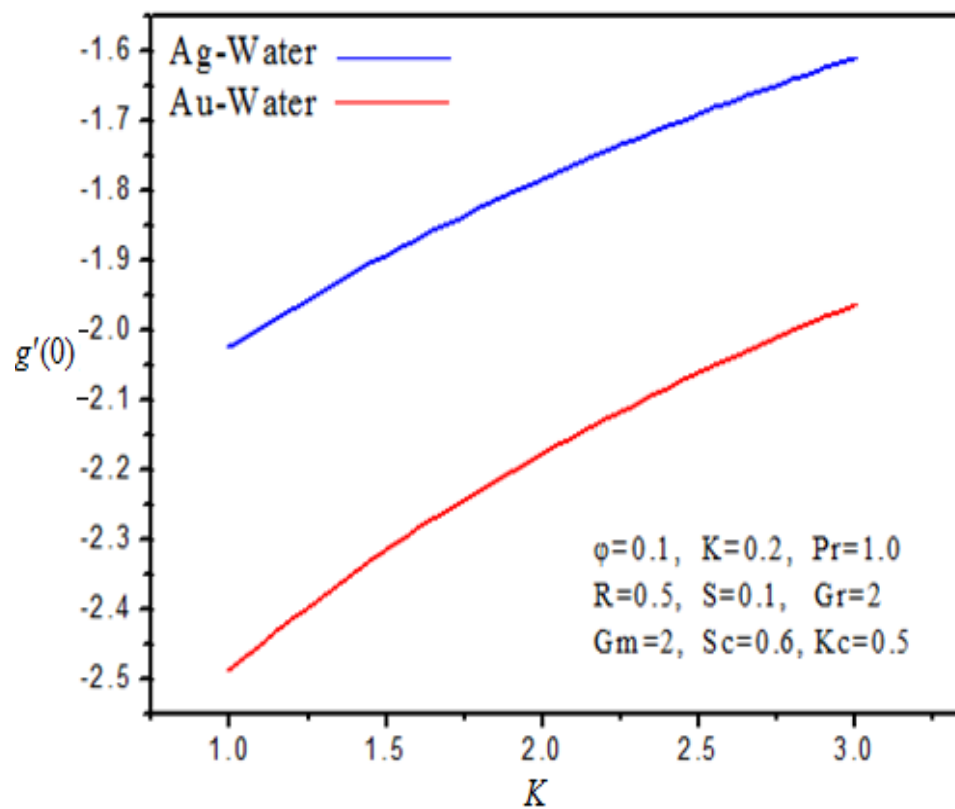


Figure 27: Effect of K on wall couple stress coefficient for silver and gold water nanofluids

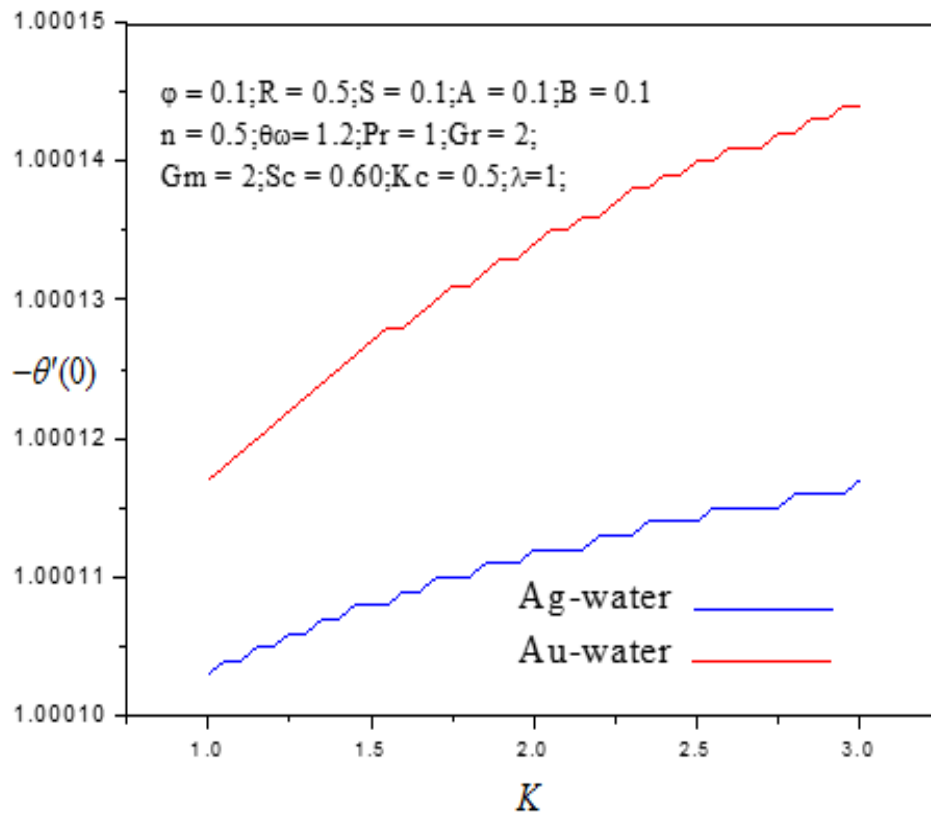


Figure 28: Effect of K on Nusselt number for silver and gold water nanofluids

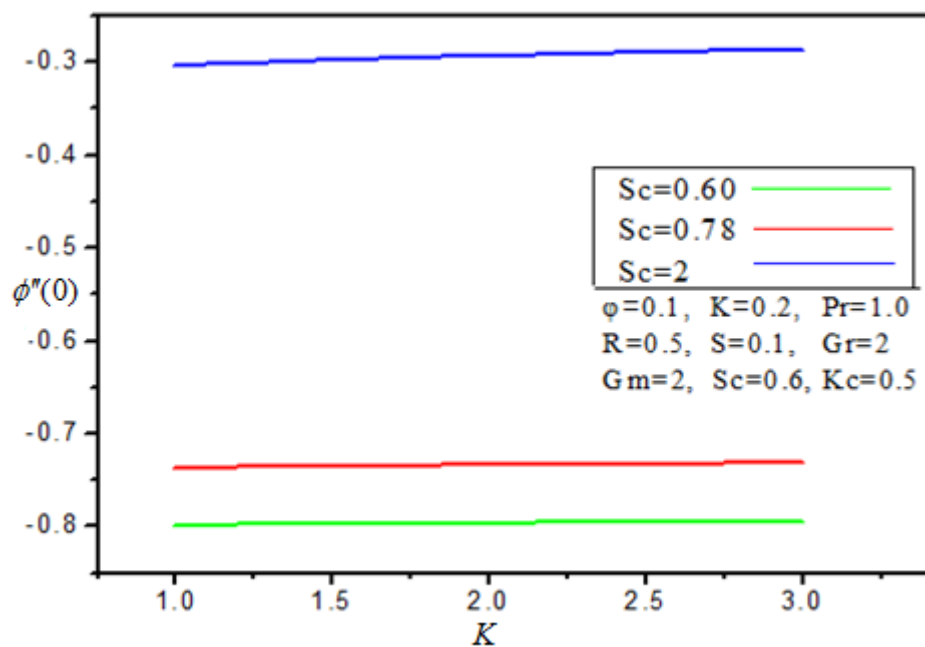


Figure 29: Effect of K and Schmidt number on Sherwood number for silver water nanofluid

Table 2: Comparison of skin friction, couple stress and Nusselt number function for nanoparticle volume fraction and Eringen micropolar parameters and Ag-water nanofluid

φ	K	$f''(0)$	$g'(0)$	$\theta'(0)$
Ag-Water				
0	0	-2.965126	-1.916728	-1.000112
0	1	-2.313070	-1.565457	-1.000126
0.1	0	-3.919752	-2.341695	-1.00089
0.1	1	-3.024650	-1.968143	-1.000105
0.2	0	-4.235559	-2.565103	-1.000073
0.2	1	-3.400666	-2.227891	-1.000089

Table 3: Comparison of skin friction, couple stress and Nusselt number function for nanoparticle volume fraction and Eringen micropolar parameters and Au-water nanofluid

φ	K	$f''(0)$	$g'(0)$	$\theta'(0)$
Au-Water				
0	0	-2.965136	-1.916735	-1.000152
0	1	-2.313077	-1.565464	-1.000170
0.1	0	-5.286651	-3.008696	-1.000078
0.1	1	-3.848190	-2.486851	-1.000117
0.2	0	-6.474936	-3.381279	-1.000040
0.2	1	-4.778112	-2.911877	-1.000085

Table 4: Comparison of skin friction, couple stress and Nusselt number function for nanoparticle volume fraction and Eringen micropolar parameters and Cu-water nanofluid

φ	K	$f''(0)$	$g'(0)$	$\theta'(0)$
Cu-Water				
0	0	-2.965128	-1.916729	-1.000120
0	1	-2.313071	-1.565458	-1.000135
0.1	0	-3.687992	-2.2999500	-1.000101
0.1	1	-2.877727	-1.935179	-1.000118
0.2	0	-3.886682	-2.398400	-1.000093
0.2	1	-3.160552	-2.091480	-1.000109

With increasing Gr values the flow is significantly accelerated and a strong overshoot is generated near the sheet surface for all cases of blowing ($S < 0$) but only for strong buoyancy with suction ($Gr = 2, S > 0$). This is displaced further from the wall with stronger thermal

buoyancy effect. Minimum velocity corresponds to the forced convection flow case ($Gr = 0$). Generally significant acceleration is induced with increasing wall blowing (injection) i.e. $S < 0$ whereas retardation is generated with wall suction ($S > 0$). Mass flux out of the boundary layer regime causes stronger adherence to the wall and opposes momentum development leading to deceleration. The contrary response is caused with blowing (mass injection into the boundary layer). i.e. momentum (hydrodynamic) boundary layer thickness is enhanced. Asymptotically smooth profiles are consistently attained in the free stream confirming that an adequately large infinity boundary condition has been deployed in the simulations. **Fig. 3** shows that micro-rotation (angular velocity) is strongly accentuated with increasing thermal Grashof number. Substantially greater magnitudes are computed with blowing compared with suction. Generally smooth decays are computed from the wall (sheet surface) into the free stream except for the case of forced convection ($Gr = 0$) with suction ($S = 0.5$) for which a monotonic growth is observed and closer to the wall reverse spin is induced (negative microrotation). Microelement spin is overall assisted with thermal buoyancy and injection indicating that natural convection and mass influx into the boundary layer encourage gyratory motions of the microelements. Despite the absence of the thermal buoyancy effect in the microrotation conservation eqn. (14) nevertheless there is a very strong coupling between the angular velocity (g) and linear velocity (f) fields via the terms, fg' , $-f'g$, $-K/L_2(2g + f'')$ in eqn (14) and the other coupling term, $(K/L_2)g'$ in the linear momentum eqn. (13). The influence of thermal buoyancy term in eqn. (13) i.e. $+Gr \theta$ is therefore considerable. **Fig. 4** indicates that there is a marked depletion in temperatures with increasing Gr values. Significantly larger temperature magnitudes are observed for injection ($S < 0$) compared with suction ($S > 0$). The convection currents which are exacerbated with greater thermal buoyancy (larger Gr), accelerate the flow but simultaneously redistribute heat in the regime. Hotter fluid is replaced by cooler fluid which results in a thinner thermal boundary layer thickness. Noticeably greater temperatures are computed with injection compared with suction, indicating that the former increases thermal boundary layer thickness whereas the latter reduces it. **Fig. 5** reveals that indicates nanoparticle concentration values (ϕ) are also suppressed with increasing Grashof numbers. Higher magnitudes are observed for injection compared with suction. The species buoyancy force, $+Gm\phi$ in the momentum eqn. (13) (where Gm is the solutal Grashof number) couples the velocity field with the nanoparticle diffusion field i.e., eqn. (16). The latter is also coupled to the linear momentum eqn. (13) via the term, $+Sc f \phi'$. Nanoparticle concentration boundary layer thickness is reduced with stronger thermal buoyancy force. The prescription of a Schmidt number of 0.6 also indicates that momentum diffusion rate is exceeded by species diffusion rate which results in a thinner concentration boundary layer thickness compared with momentum boundary layer thickness.

Figs. 6-9 illustrate the response in linear velocity, temperature, angular velocity (micro-rotation) and nanoparticle concentration profiles with various solutal Grashof number (Gr) and wall suction (S) parameter values. Similar responses are induced to those observed with a change in thermal Grashof number, described earlier. A pronounced velocity overshoot (Fig. 6) accompanies a rise in Gm values with wall injection present ($S = -.05$). This velocity shoot migrates further from the wall with increasing Gm values. It is however only present for the strongest case of species buoyancy ($Gm = 2$) when suction is imposed at the wall ($S = 0.5$). With species buoyancy absent ($Gm = 0$), or weak ($Gm = 1$) i.e., species buoyancy and viscous forces equal), the velocity overshoot vanishes, and this is a classical result which has been confirmed experimentally by Gebhart *et al.* [70]. Effectively increasing species buoyancy accelerates the flow both with either injection or suction present at the wall. Flow reversal is

never induced anywhere in the boundary layer indicating that no separation effects are present and laminar flow control is maintained. Increasing species Grashof number also induces a strong enhancement in microrotation (Fig. 7), and spin of microelements is consistently minimized for the non-buoyancy case ($Gm = 0$) for both suction or injection at the wall. As in the case of thermal Grashof number, monotonic decays from the wall to the free stream are observed for all cases except for $Gm = 0$ with suction at the wall. This deviates from the general behavior and exhibits a monotonic growth from the wall. Nevertheless, the overwhelming impact of species buoyancy force is to accelerate the spin of microelements, in particular, in close proximity to the wall, and to *increase* angular momentum boundary layer thickness. A similar observation has been reported by several other investigators including Pal and Mandal [54] and Kumar *et al.* [56], although they neglected chemical reaction effects in their analyses and considered much higher Prandtl numbers. Figs. 8 and 9 indicate that both temperature and nanoparticle concentrations are decreased with increasing species Grashof number, Gm , although the magnitudes are somewhat higher for temperatures than concentrations. Again, there is a suppression in both with increasing suction whereas the reverse effect is sustained with wall injection. Thermal boundary layer and nanoparticle concentration boundary layer thicknesses are substantially reduced with increasing species buoyancy force effect.

Figs. 10-12 illustrate the response in linear velocity, angular velocity (micro-rotation) and temperature with micropolar wall parameter, n . The case of very weak suction, $S = 0.1$ is set as the default. The parameter, n , features solely in the wall angular velocity boundary condition (17) i.e., $g(0) = -n f''(0)$. Soundalgekar and Takhar [71] has shown that n represents microelement concentration difference. When $n = 0$ heavy microelement concentration arises at the boundary implying that the micro-elements are crowded and unable to spin near the wall, $n = (1/2)$ denotes weak microelement concentration (the usual scenario for laminar boundary layers) and $n \geq$ broadly applies to more intense flows and in the extreme to turbulent boundary layer flows. There is a significant elevation in linear velocity (Fig. 10) with increasing n values. This applies to both the case of injection (dashed lines) and suction (solid lines), although significantly greater velocity magnitudes correspond to the former case. The profiles are inverted parabolas in all cases. The strong microelement concentration scenario at the wall ($n = 0$) stifles momentum development in the boundary layer and increases momentum boundary layer thickness. Increasing the microrotation boundary condition parameter, n , clearly exerts a positive influence on boundary layer flow and generally reduces momentum boundary layer thickness, encouraging faster shearing at the wall. There is also an enhancement in microrotation values (Fig. 11) with increasing n values, although the topology of profiles is now of the form of monotonic decays from the wall to the freestream. Evidently with progressively less dense concentrations of microelements at the wall, the microelements are able to spin more freely (more space in the boundary layer regime is available), and gyratory motions are accentuated. For the strong microelement wall case ($n = 0$) angular velocity is practically eliminated. Angular momentum boundary layer thickness is therefore generally reduced with greater values of the parameter, n . Again, injection (dashed lines) induces greater microelement spin (microrotation) compared with suction (solid lines). Fig. 12 shows that there is a linear decay in temperature from the sheet surface (wall) to the free stream for all values of n . Increasing n leads to a weak reduction in temperatures and this is characteristic of the cooling properties of purely micropolar fluids, as noted in [72], although the rigid elements do not interact with the nanoparticles in suspension nor do they inhibit the thermal enhancement behavior of nanoparticles. Thermal boundary layer thickness is diminished with the increasing microrotation boundary condition parameter, n , and the reduction is stronger with injection at the wall as compared with suction.

Figs. 13-15 illustrate the response in linear velocity, angular velocity (micro-rotation), temperature for Au-water and Ag-water nanofluids with suction (since this is associated with stabilizing materials processing regimes). The case $S = 0$ corresponds to a solid wall i.e., absence of lateral mass flux. With increasing suction, as noted earlier, there is a strong deceleration in the flow (Fig. 13). Au-water (gold) micropolar nanofluid achieves *marginally greater* velocity magnitudes than the Ag-water (silver) case near the wall, whereas this trend is reversed further into the boundary layer regime. For zero or low suction ($S = 0, 0.5$) a velocity overshoot is observed near the wall, which vanishes for higher values of suction ($S = 1, 2$) owing to the greater adherence of the boundary layer to the wall (sheet boundary) which destroys momentum. Asymptotically smooth decays are computed in all cases towards the free stream. Maximum velocity is associated with the Au-water for a solid wall ($S = 0$) and the minimum velocity computed is also for Au-water but at maximum wall suction ($S = 2$). Fig. 14 shows that for suction parameter values, S , up to 1, the microrotation profiles descend from a maximum at the wall to the free stream, for both Ag-water and Au-water cases. However, for strong suction ($S = 2$), the profiles ascend from a minimum at the wall to vanish in the free stream. In this scenario reverse microelement spin is computed indicating that strong suction induces a significant impact on the gyratory motion direction. In this case Au-water microrotation values are lower than for Ag-water micropolar nanofluid, whereas for all other suction cases, Au-water achieves higher micro-rotation values than Ag-water. Fig. 15 indicates that increasing suction depresses temperatures throughout the boundary layer. There is a marginally greater temperature computed for Ag-water compared with Au-water for the solid wall case ($S = 0$). As elaborated earlier, thermal boundary layer thickness is significantly decreased with stronger suction.

Fig. 16 visualizes the variation in nanoparticle concentration profiles ($\phi(\eta)$) for various Schmidt numbers (Sc) variation and for gold, silver and copper-water micropolar nanofluids. No tangible modification in concentration values is computed for the different metallic nanoparticles. With increasing Schmidt number however, there is a substantial depletion in nanoparticle concentration and concentration boundary layer thickness is also reduced. This key parameter in convective mass transfer parameter symbolizes the *ratio of the momentum to the mass diffusivity*. It measures the relative effectiveness of momentum and mass transport by diffusion in the hydrodynamic (velocity) and concentration (nanoparticle species) boundary layers. $Sc = 1.0$ corresponds to both momentum and species boundary layer thicknesses being the same. In the present investigation we consider $Sc < 1$, for species diffusivity exceeds momentum diffusivity and this range is appropriate for aqueous polymers. For $Sc > 1$ momentum diffusion rate exceeds the species molecular diffusion rate. Mass diffusivity or diffusion coefficient is a proportionality constant between the molar flux due to molecular diffusion and the gradient in the concentration of the species (or the driving force for diffusion). Schmidt number therefore allows engineers an insight into the selection of different molecular diffusivities corresponding to different nanoparticles in nanofluid suspensions. Larger Schmidt numbers leads to a thinning in the concentration boundary layer. With thinner concentration boundary layers, the concentration gradients will be enhanced causing a decrease in concentration of species in the boundary layer. The implication for engineering designers is that in such a regime, a diffusing nanoparticle species with a *lower Schmidt number* is more amenable to achieving enhanced nanoparticle concentration distributions.

Figure 17 depicts the nanoparticle concentration distribution with first order chemical reaction parameter, Kc . The formulation in Eqn. (16) corresponds to a *homogenous destructive reaction* when $Kc > 0$ and a *homogenous constructive reaction* when $Kc < 0$. In the former more nanoparticles are converted to a new species (destructive) whereas in the latter less nanoparticles are transformed (constructive). In consistency with this chemo-physics, we

observe that nanoparticle concentration is boosted for $Kc = -0.1$ and -0.5 whereas it is reduced with $Kc = 0.1, 0.5$. The case $Kc = 0$ corresponds to non-reactive flow of micropolar nanofluid. Destructive reactions therefore lead to an enhancement in nanoparticle species boundary layer thickness whereas the opposite effect is induced for constrictive chemical reactions. Smooth monotonic decays are again computed for all cases from the wall to the edge of the boundary layer (free stream), confirming that a sufficiently large infinity boundary condition has been used.

Figs. 18-21 present the evolution in linear velocity, angular velocity (micro-rotation), temperature and nanoparticle concentration profiles with various Eringen micropolar material parameter values (K) and nanoparticle volume fractions (ϕ) for Au-water micropolar nanofluids. The Eringen parameter features extensively in both the linear momentum (13) (i.e., in the terms, $\{((L_1 + K)/L_2) f''', +(K/L_2) g'\}$) and angular momentum (14) (i.e., the terms $\{((L_1 + (K/2))/L_2) g'', -K/L_2(2g + f'')\}$) conservation equations and is often known as the “micropolar coupling parameter”. Initially a reduction in velocity is induced with increasing K values, in particular near the wall. With further distance into the boundary layer, however this trend is reversed, and significant acceleration is observed which is sustained into the free stream. With $K = 1$ micropolar vortex viscosity and Newtonian dynamic viscosity are exactly equal. With $K > 1$ the vortex viscosity exceeds the dynamic viscosity which alters the momentum transfer in the flow and generally produces acceleration, confirming the drag-reducing properties of micropolar fluids. Increasing volume fraction initially enhances velocity magnitudes closer to the wall whereas with progression into the boundary layer it results in strong deceleration. Fig. 19 demonstrates that microrotation, $g(\eta)$ is reduced with increasing micropolar parameter, K , Angular momentum boundary layer thickness is reduced. However increasing nanoparticle volume fraction is observed to elevate microrotation i.e. greater doping with nanoparticles assists the spin of microelements. Fig. 20 shows that although initially temperature is increased with micropolar parameter, K , the dominant effect is for temperature reduction i.e. cooling of the regime. Increasing nanoparticle volume fraction however strongly enhances temperatures and increases the thermal boundary layer thickness, a characteristic of nanoparticle suspensions. Greater presence of high thermal conductivity metallic nanoparticles (gold) enhances the overall thermal conductivity of the micropolar nanofluid which elevates temperatures. Fig. 21 shows that significant elevation in nanoparticle concentration is achieved with increased volume fraction, (ϕ). In all cases the profiles are linear growths. Higher values of Eringen micropolar parameter, K , however, suppress the nanoparticle concentration magnitudes. The acceleration in linear and angular flow encourages momentum diffusion rather than species diffusion, which results in a reduction in nanoparticle concentration boundary layer thickness with stronger micropolar vortex viscosity.

Figs. 22-25 present the corresponding plots for Ag-water micropolar nanofluid. Generally similar trends are computed although there tends to be a larger dispersion in the profiles of temperature (Fig. 23) and micro-rotation (Fig. 24). In other words, increasing micropolar parameter basically accelerates the linear flow, suppresses the microrotation, reduces temperatures and also nanoparticle concentrations whereas increasing nanoparticle volume fraction elevates temperatures (higher values are obtained than in the Au-water case) and nanoparticle concentration magnitudes in the Ag-water case.

Figs. 26-29 illustrate the impact of the Eringen micropolar parameter, K for both Ag-water micropolar nanofluid on the skin friction, couple stress, Nusselt number function and Sherwood number, for volume fraction of 10% ($\phi = 0.1$) with wall suction present ($S = 0.1$) and weak radiative flux ($R = 0.1$). Skin friction is greatly increased with K values, confirming the acceleration achieved with stronger micropolarity and the drag-reducing properties of

micropolar nanofluids. Substantially greater skin friction is achieved with Ag-water compared with Au-water. Couple stress magnitudes are also elevated with increasing micropolar parameter, K and much higher magnitudes correspond to Ag-water rather than Au-water. Fig. 27 reveals that Ag-water achieves lower Nusselt numbers (at any value of micropolar parameter, K) compared with Au-water. Silver nanoparticles possess the highest thermal conductivity of any element and the highest light reflectance. Since silver is the best thermal conductor, this enhances temperatures in the boundary layer and draws heat away from the wall (sheet). Heat transfer to the wall is therefore lowered and this manifests in lower Nusselt numbers. Conversely gold has a lower thermal conductivity than silver and achieves lower temperatures in the main body of the micropolar nanofluids, which is due to greater heat transfer to the wall i.e. larger Nusselt numbers. Although silver has superior thermal conductivity, it is noteworthy that gold, despite being more expensive, has a much higher corrosion resistance and is therefore of considerable interest in nanomaterials processing for achieving enhanced durability in coatings. Increasing micropolar parameter consistently elevates the Nusselt number for both Ag-water and Au-water, since stronger micropolarity cools the micropolar nanofluids (higher vortex viscosities) with enhanced convection away from the fluid to the wall (higher Nusselt number). Finally, Fig. 29 shows that with increasing micropolar parameter, K , there is a slight enhancement in Sherwood number i.e., greater nanoparticle mass transfer to the wall. However, a much more prominent elevation is achieved with increasing Schmidt number since this is inversely proportional to the mass diffusivity of the nanoparticles whereas micropolar parameter is related only to vortex and dynamic viscosities.

Tables 2-4 present skin friction, couple stress and Nusselt number function for nanoparticle volume fraction and Eringen micropolar parameters and Ag-water nanofluid. Tables 2 and 3 confirm the graphical results presented earlier. Table 4 also shows that with increasing micropolar parameter, K , skin friction, couple stress and Nusselt number are all reduced. With increasing nanoparticle volume fraction both skin friction and couple stress are substantially increased whereas Nusselt number is weakly decreased. Comparing all three Tables, the higher skin friction and couple stress magnitudes are associated with Au-water, then Ag-water and the lowest with Cu-water. However in all three cases the Nusselt numbers are of the same order.

6. CONCLUSIONS

A detailed mathematical and numerical study of thermo-solutal natural convection chemically reacting micropolar nanofluid flow from a permeable stretching surface with non-uniform heat source/sink has been presented. Radiative heat transfer has also been considered. The rheological and nanoscale characteristics have been modelled by combining the Tiwari-Das nanofluid formulation with the Eringen micro-morphic model. The study is motivated by simulating Sakiadis flow in high-temperature nanomaterials processing. The transformed ninth ordinary differential equation boundary value problem has been solved with Runge-Kutta 45 Fehlberg method (Maple **dsolve routine**). Several nanoparticles i.e. gold, silver or copper with aqueous base fluid have been investigated. Validation of solutions with earlier non-reactive studied in the absence of nanoparticle mass transfer has also been conducted. The present computations have shown that:

- Increasing volume fraction decreases velocity whereas it elevates microrotation, temperature and nanoparticle concentration.
- Gold (Au)-water micropolar nanofluids achieves highest skin friction and couple stress magnitudes, then Silver (Ag)-water and finally Copper (Cu)-water.
- Increasing nanoparticle volume fraction enhances both skin friction and couple stress but marginally reduces the Nusselt number.

- Increasing micropolar parameter, K , significant acceleration is induced (greater linear velocities), whereas angular velocity (microrotation), temperature and nanoparticle concentration.
- Nanoparticle concentration (and nanoparticle species boundary layer thickness) are elevated for stronger destructive chemical reaction effect (negative reaction parameter values) whereas they are suppressed with constructive chemical reaction.
- Increasing Schmidt number generates a significant reduction in nanoparticle concentration and concentration boundary layer thickness.
- Generally increasing wall injection accelerates the flow and accentuates angular velocity (microrotation). However, increasing suction decreases temperatures and a slightly higher temperature is obtained for Eqs. -water compared with Au-water for the solid wall case (zero wall transpiration).
- With greater micropolar boundary condition parameter (“surface parameter”), the velocity is elevated, microrotation but reduces temperature and thermal boundary layer thickness.

The present simulations have been confined to steady-state conditions and metallic nanoparticles. Future investigations will consider carbon nanotubes (CNTs) [73] and unsteady effects and will be reported imminently.

REFERENCES

- [1] Chhabra, R. P. and J. Richardson, J., 2008. **Non-Newtonian Flow and Applied Rheology**. Butterworth-Heinemann, USA.
- [2] Jaluria, Y., 1996. Heat and mass transfer in the extrusion of non-Newtonian materials. **Adv. Heat Transf**, **28**, pp. 145-230.
- [3] Lee, J. and Nam, J., 2016. A simple model for viscoplastic thin film formation for coating flows. **J. Non-Newtonian Fluid Mech**, **229**, pp. 16-26.
- [4] Saad, A., Echchelh, A., Hattabi, M., El Ganaoui, M. and Lahlou, F., 2012. Numerical simulation and analysis of flow in resin transfer moulding process. **Fluid Dyn. Mat. Proc**, **8(3)** pp. 277-294.
- [5] Khan, Z., Rasheed, H. U., Alharbi, S. O., Khan, I., Abbas, T. and Chin, D. L. C., 2019. Manufacturing of double layer optical fiber coating using Phan-Thien-Tanner fluid as coating material. **Coatings**, **9**, 147. <https://doi.org/10.3390/coatings9020147>
- [6] Zevallos, G. A., Carvalho, M. S. and Pasquali, M., 2005. Forward roll coating flows of viscoelastic liquids. **J. Non-Newtonian Fluid Mech**, **130**, pp. 96-109.
- [7] Chang, T. B., Mehmood, A., **Anwar Bég, O.**, Narahari, M., Islam, M. N. and Ameen, F., 2011. Numerical study of transient free convective mass transfer in a Walters-B viscoelastic flow with wall suction. **Commun. Nonlinear Sci. Numer. Simult**, **16**, pp. 216-225.
- [8] Garg, V. K. and Rajagopal, K. R., 1991. Flow of a non-Newtonian fluid past a wedge. **Acta Mech**, **88**, pp. 113–123.

- [9] Eringen, A. C., 1967. Theory of micropolar fluids. **J. Math. Mech**, **16**, pp. 1–18.
- [10] **Anwar Bég, O.**, Bhargava, R., Rashidi., M. M., 2011. Numerical Simulation in Micropolar Fluid Dynamics, Lambert, (288 pages).
- [11] Hung, C. I., Tsai, J. S. and Chen, C. K., 1996. Nonlinear stability of the thin micropolar liquid film flowing down on a vertical plate. **ASME J. Fluids Eng**, **118**, pp. 498–505.
- [12] Gupta, D., Kumar, L., **Anwar Bég O.** and Singh, B., 2014. Finite element simulation of mixed convection flow of micropolar fluid over a shrinking sheet with thermal radiation. **Proc IMechE- Part E: J. Proc. Mech. Eng**, **228(1)**, pp. 61-72.
- [13] Chen, C. K., Lin, M. C., Chen, C. I., Stability analysis of a thin micropolar fluid flowing on a rotating circular disk. **J. Mech**, **27**, pp. 95-105.
- [14] Shamshuddin, MD., Sheri, S. R. and **Anwar Bég, O.**, 2017. Oscillatory dissipative conjugate heat and mass transfer in chemically reacting micropolar flow with wall couple stress: A finite element numerical study. **Proc. IMechE Part E: J Proc. Mech. Eng**, **223(1)**, pp. 48-64.
- [15] Sheremet, M. A., Pop, I. and Ishak, A., 2017. Time-dependent natural convection of micropolar fluid in a wavy triangular cavity. **Int. J. Heat and Mass Transf**, **105**, pp. 610-622.
- [16] Madhavi, K., Prasad, V. R., Rao, A. S., **Anwar Bég, O.** and Kadir, A., 2018. Numerical study of viscoelastic micropolar heat transfer from a vertical cone for thermal polymer coating. **Nonlinear Eng**, (13 pages) <https://doi.org/10.1515/NLENG-2018-0064> REC
- [17] Chiu, C. P., Shich, J. Y. and Chen, W. R., 1999. Transient natural convection of micropolar fluids in concentric spherical annuli. **Acta Mech**, **132**, pp. 75–92.
- [18] Chaube, M. K., Yadav, A., Tripathi, D. and **Anwar Bég, O.**, 2018. Electroosmotic flow of biorheological micropolar fluids through microfluidic channels. **Korea-Australia Rheology J**, **30(2)**, pp. 89-98.
- [19] Ali, N., Asghar, Z. and **Anwar Bég, O.**, 2018. A mathematical model of bacterial gliding on a thin layer of micropolar slime. **Results in Phys**, **9**, pp. 682-691.
- [20] Srinivas, J. and **Anwar Bég, O.**, 2018. Homotopy study of entropy generation in magnetized micropolar flow in a vertical parallel plate channel with buoyancy effect. **Heat Transf Res**, **49(6)**, pp. 529–553.
- [21] Akbar, N. S., Tripathi, D., Khan, Z. H. and **Anwar Bég, O.**, 2018. Mathematical modelling of pressure-driven micropolar biological flow due to metachronal wave propulsion of beating cilia. **Math. Biosci**, **301**, pp. 121-128.
- [22] **Anwar Bég, O.**, Ferdows, M., Karim, M. E., Hasan, M. M., Beg, T. A., Shamshuddin, MD. and Kadir, A., 2020. Computation of non-isothermal thermo-convective micropolar fluid

dynamics in a Hall MHD generator system with non-linear distending wall. **Int. J. Appl. Comput. Math**, **6**, **42**. <https://doi.org/10.1007/s40819-020-0792-y>

[23] Hiremath, A., Reddy, G. J., **Anwar Beg, O.**, 2019. Transient analysis of third-Grade viscoelastic nanofluid flow external to a heated cylinder with buoyancy effects. **Arabian J. Sci. Eng**, **44(9)**, pp. **7875-7893**.

[24] Hiremath, A., Reddy, G. J., Kumar, M., **Anwar Beg, O.**, 2019. Unsteady free convective heat transfer in third-grade fluid flow from an isothermal vertical plate: A thermodynamic analysis. **Int. J. Mod. Phys. B**, **33**, **1950060**. <https://doi.org/10.1142/S0217979219500607>

[25] Reddy, G. J., Hiremath, A., Kumar, M., 2018. Computational modeling of unsteady third-grade fluid flow over a vertical cylinder: A study of heat transfer visualization. **Results in Phys**, **8**, pp. **671-682**.

[26] Chand, R., Yadav, D., Bhattacharya, K., Awasthi, M. K., 2021. Thermal convection in a layer of micropolar nanofluid. **Asia-Pacific J. Chem. Eng**, **16(5)**, **e2681**. <https://doi.org/10.1002/apj.2681>

[27] Yadav, D., Wang, J., 2019. Convective heat transport in a heat generating porous layer saturated by a non-Newtonian nanofluid. **Heat Transf. Eng**, **40(16)**, pp. **1363–1382**.

[28] Yadav, D., 2019. The onset of longitudinal convective rolls in a porous medium saturated by a nanofluid with non-uniform internal heating and chemical reaction. **J. Therm. Anal. Calorim**, **135**, pp. **1107–1117**.

[29] Choi, S. U. S., 1995. Enhancing thermal conductivity of fluids with nanoparticles, In *Developments and Applications of Non-Newtonian Flows*, Edited by: Singer, D. A. and Wang, H. P., **New York: American Society of Mechanical Engineers, FED 231**, pp. **99–105**.

[30] Tiwari, R. K., and Das, M. K., 2007. Heat transfer augmentation in a two-sided lid-driven differentially heated square cavity utilizing nanofluids. **Int. J. Heat Mass Transf**, **50**, pp. **2002–2018**.

[31] Buongiorno, J., 2006. Convective transport in nanofluids. **ASME J. Heat Transf**, **128 (3)**, pp. **240–250**.

[32] Huang, S., Li, X., Yu, B., Jiang, Z. and Huang, H., Machining characteristics and mechanism of GO/SiO₂ nano-slurries in fixed abrasive lapping. **J. Mat. Proc. Tech**, **277**, **116444**. <https://doi.org/10.1016/j.jmatprotec.2019.116444>.

[33] Chandradass, J., Han, K. S. and Bae, D. S., 2008. Synthesis and characterization of zirconia- and silica-doped zirconia nano-powders by oxalate processing. **J. Mat. Proc. Tech**, **206**, pp. **315-321**.

- [34] Chang, H. and Chang, Y. C., 2008. Fabrication of Al_2O_3 nanofluid by a plasma arc nanoparticles synthesis system. **J. Mat. Proc. Tech**, **207**, pp. 193-199.
- [35] <https://www.nasiol.com> (2020).
- [36] Uddin, M. J., Khan, W. A., **Anwar Bég, O.** and Ismail, A. I. M., 2020. Non-similar solution of g-jitter induced unsteady magnetohydrodynamic radiative slip flow of nanofluid. **Appl. Sci**, **10**, 1420 (17 pages). <https://doi.org/10.3390/app10041420>
- [37] Hayat, T., Khan, M. I., Farooq, M., Alsaedi, A., Waqas, M. and Yasmeen, T., 2016. Impact of Cattaneo–Christov heat flux model in flow of variable thermal conductivity fluid over a variable thickness surface. **Int. J. Heat Mass Transf**, **99**, pp. 702–710.
- [38] Bhatti, M. M., Khalique, C. M., Bég, T. A., **Anwar Bég, O.** and Kadir, A., 2020. Numerical study of slip and radiative effects on magnetic Fe_3O_4 -water-based nanofluid flow from a nonlinear stretching sheet in porous media with Soret and Dufour diffusion. **Modern Phys Let B**, **33**, 2050026 (24 pages). <https://doi.org/10.1142/S0217984920500268>.
- [39] Maghsoudi, K., Jafari, R., Momen, G., Farzaneh, M., 2017. Micro-nanostructured polymer surfaces using injection molding: A review. **Mater. Today Commun**. **13**, pp. 126–143.
- [40] Naik, B. A. K. and Vinod, A. V., 2018. Heat transfer enhancement using non-Newtonian nanofluids in a shell and helical coil heat exchanger. **Exper. Therm. Fluid Sci**, **90**, pp. 132-142.
- [41] Kumar, M., Reddy, G. J., Kumar, N. N. and **Anwar Bég, O.**, 2019. Computational study of unsteady couple stress magnetic nanofluid flow from a stretching sheet with Ohmic dissipation. **Proc. IMechE-Part N: J Nanoeng. Nanomat. Nanosyst**, **233(2-4)**, pp. 49-63.
- [42] Dubey, A., Vasu, B., **Anwar Bég, O.** and Gorla, R. S. R., 2020. Numerical simulation of two-fluid non-Newtonian nano-hemodynamics through a diseased artery with a stenosis and aneurysm. **Computer Methods in Biomech. Biomed Eng**, pp. 1-27.
<https://doi.org/10.1080/10255842.2020.1729755>
- [43] Ray, A. K., Vasu, B., **Anwar Bég, O.**, Gorla, R. S. R. and Murthy, P. V. S. N., 2019. Homotopy semi-numerical modelling of non-Newtonian nanofluid transport external to multiple geometries using a revised Buongiorno model, **Inventions**, **4(4)**, pp. 1-27.
- [44] Lund, L. A., Omar, Z., Khan, U., Khan, I., Baleanu, D., Nisar, K. S., 2020. Stability analysis and dual solutions of micropolar nanofluid over the inclined stretching/shrinking surface with convective boundary condition, **Symmetry**, **12(1)**, 74.
<https://doi.org/10.3390/sym12010074>

- [45] Gaffar, S. A., **Anwar Bég, O.**, Prasad, V. R., 2018. Mathematical modelling of natural convection in a third grade viscoelastic micropolar fluid from an isothermal inverted cone. **J. Sci. Tech. Trans. Mech. Eng.** **44**, pp. 383-402.
- [46] Das, K. and Duari, P. K., 2017. Micropolar nanofluid flow over a stretching sheet with chemical reaction. **Int. J. Appl. Comput. Math**, **3**, pp. 3229–3239.
- [47] Hussanan, A., Salleh, M. Z., Khan, I. and Shafie, S. 2017. Convection heat transfer in micropolar nanofluids with oxide nanoparticles in water, kerosene and engine oil. **J. Mol. Liq**, **229**, pp. 482-488.
- [48] Prasad, V. R., Gaffar, S. A. and **Anwar Bég, O.**, 2015. Heat and mass transfer of a nanofluid from a horizontal cylinder to a micropolar fluid. **AIAA J. Thermophys. Heat Transf**, **29(1)**, pp. 127-139.
- [49] Shah, Z., Islam, S., Gul, T., Bonyah, E., Khan, M. A., 2018. The electrical MHD and Hall current impact on micropolar nanofluid flow between rotating parallel plates. **Results in Phys**, **9**, pp. 1201-1214.
- [50] Latiff, N. A., Uddin, M. J., **Anwar Bég, O.** and Ismail, A. I. M., 2016. Unsteady forced bioconvection slip flow of a micropolar nanofluid from a stretching/shrinking sheet. **Proc. IMechE-Part N: J Nanoeng. Nanomat. Nanosyst**, **230(4)**, pp. 177–187.
- [51] Bang, J., Didenko, Y., Helmich, R. and Suslick, K., 2012. Nanostructured materials through ultrasonic spray pyrolysis. **Mat. Matt**, **7(2)**, pp. 15-20.
- [52] Paulauskas, I. E., Modeshia, D. R., 2013. Photocatalytic activity of doped and undoped titanium dioxide nanoparticles synthesized by flame spray pyrolysis. **Platinum Metals Rev**, **57 (1)**, **32**. <https://doi.org/10.1595/147106713x659109>.
- [53] Kozhukharov, S., 2014. High temperature methods for the synthesis and industrial production of nanomaterials, in **Nanofabrication using Nanomaterials**, Eds. (**Jean Ebothé and W. Ahmed**) One Central Press (OCP), UK.
- [54] Pal, D. and Mandal, G., 2017. Thermal radiation and MHD effects on boundary layer flow of micropolar nanofluid past a stretching sheet with non-uniform heat source/sink, **Int. J. Mech. Sci**, **126**, pp. 308-318.
- [55] Hayat, T. and Khan, M. I., 2017. Radiative flow of micropolar nanofluid accounting thermophoresis and Brownian movement. **Int. J. Hydrogen Energy**, **42**, pp. 16821-16833.
- [56] Kumar, B., Seth, G. S., Nandkeolyar, R., 2019. Regression model and successive linearization approach to analyze stagnation point micropolar nanofluid flow over a stretching sheet in a porous medium with nonlinear thermal radiation. **Phys. Scr.**, **94**, 115211. <https://doi.org/10.1088/1402-4896/ab2078>.

- [57] Shah, Z., Khan, A., Khan, W., Alam, M. K., Islam, S., Kumam, P. and Thounthong, P., 2020. Micropolar gold blood nanofluid flow and radiative heat transfer between permeable channels. **Computer Methods and Programs in Biomedicine**, **186**, 105197. <https://doi.org/10.1016/j.cmpb.2019.105197>
- [58] Ferdows, M., Khan, M. S., **Anwar Bég, O.**, Azad, M. A. K. and Alam, M., 2014. Numerical study of transient magnetohydrodynamic radiative free convection nanofluid flow from a stretching permeable surface. **Proc. IMechE-Part E: J. Proc. Mech. Eng**, **228(3)**, pp. 181-196.
- [59] Mohapatra, D. K., Mishra, S. R. and Jena, S., 2019. Cu-water and Cu-kerosene micropolar nanofluid flow over a permeable stretching sheet. **Heat Transf Asian Res**, **48(6)**, pp. 2478-2496.
- [60] Brinkman, H., 1952. The viscosity of concentrated suspensions and solutions. **J. Chem. Phys**, **20**, pp. 571-581.
- [61] Khanafer, K., Vafai, K. and Lightstone, M., 2003. buoyancy-driven heat transfer enhancement in a two-dimensional enclosure utilizing nanofluids. **Int. J. Heat Mass Transf**, **46**, pp. 3639-3653.
- [62] Sidra, A., Khan, I., Ismail, Z. and Salleh, M. Z., 2018. Impacts of gold nanoparticles on MHD mixed convection Poiseuille flow of nanofluid passing through a porous medium in the presence of thermal radiation, thermal diffusion and chemical reaction. **Neural Comput & Applic**, **30(3)**, pp. 789-797.
- [63] Pal, D. and Chatterjee, S., 2010. Heat and mass transfer in MHD non-Darcian flow of a micropolar fluid over a stretching sheet embedded in a porous media with non-uniform heat source and thermal radiation. **Commun. Nonlinear Sci. Numer. Simlt.** **15**, pp. 1843-1857.
- [64] **Anwar Bég, O.**, Kuharat, S., Ferdows, M., Das, M., Kadir, A. and Shamshuddin, MD., 2019. Magnetic nano-polymer flow with magnetic induction and nanoparticle solid volume fraction effects: solar magnetic nano-polymer fabrication simulation. **Proc. IMechE-Part N: J Nanoeng. Nanomat. Nanosyst.** **233(1)**, pp. 27-45.
- [65] Fauzi, E. L. A., Ahmad, S. and Pop, I., 2014. Flow over a permeable stretching sheet in micropolar nanofluids with suction. **AIP Proc**, **1605**, 428. <https://doi.org/10.1063/1.4887627>.
- [66] Gorla, R. S. R., 1992. Mixed convection in a micropolar fluid from a vertical surface with uniform heat flux. **Int. J. Eng. Sci**, **30**, pp. 349-358.
- [67] **Anwar Bég, O.**, Kuharat, S., Aneja, M., Sharma, S., 2019. Numerical study of magnetic-bio-nano-polymer solar cell coating manufacturing flow. **Int. Conf. Innovative Appl. Energy (IAPE'19)**, Oxford, United Kingdom, 14-15 March.

- [68] Bergman, T. L. and Viskanta, R., 1996. Radiation heat transfer in manufacturing and materials processing, in **Radiative Transfer-I, M.P. Menguc, Editor**, Begell House, New York, (pp. 13–39).
- [69] Peddieson, J. and McNitt, R. P., 1970. Boundary layer theory for micropolar fluid. **Recent Adv. Eng. Sci**, 5, pp. 405–426.
- [70] Gebhart, B., 1988. **Buoyancy-induced Flows and Transport**, Hemisphere Publishing, Washington, USA.
- [71] Soundalgekar, V. M. and Takhar, H. S., 1983. Flow of a micropolar fluid on a continuous moving plate. **Int. J. Eng. Sci**, 21, pp. 961–965.
- [72] Bhargava, R., Sharma, S., Bhargava, P., **Anwar Bég O.** and Kadir, A., 2017. Finite element simulation of nonlinear convective heat and mass transfer in a micropolar fluid-filled enclosure with Rayleigh number effects. **Int. J. Appl. Comput. Math**, 3 (2), 1347–1379.
- [73] Akbar, N. S., Shoaib, M., Tripathi, D., Bhushan, S. and **Anwar Bég, O.**, 2018. Analytical approach for entropy generation and heat transfer analysis of CNT-nanofluids through ciliated porous medium. **J. Hydrodynam: B**, 30(2), pp. 1-11.

Acknowledgments

The authors express their sincere gratitude to the editor and reviewers for their suggestions which have improved this paper.

Nomenclature

A^*	space parameter
Ag	Silver nanoparticle
Au	Gold nanoparticle
B^*	internal heat generation or absorption parameter
c	constant
C	concentration of the solute [$mol\ m^{-3}$]
C_f	skin friction coefficient
C_w	wall couple stress
C_p	specific heat at constant pressure [$J\ Kg^{-1}K^{-1}$]
Cu	Copper nanoparticle
C_∞	free stream concentration [$mol\ m^{-3}$]
D_m	molecular diffusivity [$m^2\ s^{-1}$]
g	dimensionless microrotational velocity
g^*	acceleration due to gravity [ms^{-1}]
Gr	thermal Grashof number

G_m	solotal Grashof number
j	micro inertia per unit mass [m^2]
K	Eringen micropolar constant
Kc	chemical reaction parameter
k^*	Rosseland spectral absorption coefficient [m^{-1}]
n	microelement concentration difference
Nu	Nusselt number
Pr	Prandtl number
q_{rad}	Radiative heat flux [Wm^{-2}]
q_m	local rate of mass transfer
q_w	local rate of heat transfer
R	radiation parameter
Re_x	local Reynolds number
S	wall suction parameter
Sc	Schmidt number
Sh	Sherwood number
T	Temperature of the field in the boundary layer [K]
T_w	wall temperature of the fluid [K]
T_∞	Temperature of the fluid in free stream [K]
u	velocity component in x-direction [ms^{-1}]
U_w	stretching velocity [ms^{-1}]
v	velocity component in y-direction [ms^{-1}]
x, y	distance along and perpendicular to the plate [m]

Greek symbols

α_{nf}	thermal diffusivity of nanofluid [$m^2 s^{-1}$]
β_T	volumetric coefficient of thermal expansion [K^{-1}]
β_c	volumetric coefficient of concentration expansion [K^{-1}]
γ_{nf}	spin gradient viscosity of nanofluid [$kg ms^{-1}$]
λ	stretching constant
θ	dimensionless temperature
μ	fluid dynamic viscosity [$kg m s^{-1}$]
ν	kinematic viscosity [$m^2 s^{-1}$]
κ	Eringen vortex viscosity [$m^2 s^{-1}$]
ρ_{nf}	density of nanofluid [$kg m^{-3}$]
$(\rho c_p)_{nf}$	heat capacitance of nanofluid
σ^*	Stefan-Boltzmann constant [$Wm^{-2} K^{-4}$]
ω	dimensionless angular velocity component
ϕ	dimensionless concentration

φ	volume fraction
ψ	stream function
η	similarity variable

Subscripts

w	surface conditions
∞	conditions far away from the plate
nf	nanofluid
f	base fluid